Radio Study of Protostars

Evans Kojo Owusu
School of Physics and Astronomy
University of Leeds

A thesis submitted for the degree of

Master of Science by Research

30^{th} April, 2019.

The candidate confirms that the work submitted is his own, except where work which has formed part of jointly authored publications has been included. The contribution of the candidate and the other authors of this work has been explicitly indicated. The candidate confirms that appropriate credit has been given within this thesis where reference has been made to the work of others.

Dedication

This thesis is dedicated to men and women, government and private institutions, various funding agencies across the globe who have invested their time, resources and expertise towards the introduction, development and advancement of Radio Astronomy on the African Continent. Posterity will forever remember your act of selfless sacrifice and hard work.

Acknowledgements

I am grateful to God Almighty for giving me the inspiration that burst resilience, energy, emotional fortitude coupled with fresh and creative ideas to have key insight into how to be successful in life. Furthermore, I am eternally grateful to my supervisors, Dr. Stuart Lumsden and Professor Melvin Hoare. Their availability and patience is what has made this work largely possible and successful.

I would like to thank the Newton Fund Project- Development in Africa with Radio Astronomy (DARA) project for funding and supporting my study in the UK. In addition, a big thanks goes to Dr. Katherine Johnston and Willice Obonyo for their timely contribution and advice during the course of my research. To the astrophysics research group at Leeds University, thank you for creating a lively and conducive atmosphere during the period of my research.

To my dad and late mum, I am deeply grateful for all the wonderful opportunities you have given me in my life. If not for the sacrifices you made, I know I would not have been able to get this far. I hope that your legacy will remain with me and the generations yet unborn.

Abstract

We report radio continuum and spectral line observations of five MYSOs namely: *G310.0135+00.3892*, *G339.8838-01.2588*, *G332.9868-00.4871*, *G345.4938+01.4677* and *G345.5043+00.3480*. The objects were selected from the Red MSX Source (RMS) survey based on their bolometric luminosities and distances and were observed with the *Australia Telescope Compact Array* (ATCA). Results from the ATCA observations were compared to the H_2O southern Galactic Plane Survey (HOPS) data, extracted using the galactic coordinates of the various objects. *G345.5043+00.3480* was not detected probably because it was too extended. The observation using ATCA was carried out at 24.5 GHz observing frequency in the 1.5 km array configuration mode, achieving a resolution of $\sim$ 2 arcsec with a sensitivity range of $\sigma \sim 0.10 - 0.58$ mJy/beam for the objects. The radio continuum results were compared with previous studies by Purser (2017) for the same objects using ATCA at 22.8 GHz in the 6 km array configuration mode, achieving a resolution of 0.5 arcsec and sensitivity of $\sigma \sim 73 - 106$ μJy/beam for the objects. The luminosities of the objects were determined in the range of 1.87×10^{12} - 2.00×10^{13} W. From the spectral line emission, we report the detection of water masers in all science targets with spectral luminosities of the water masers in the range of $0.11 - 2.80 \times 10^{-6} L_{\odot}$. The water masers detected in the sources were offset on average by $\sim$ 2 km/s from the known local standard of rest velocity of the MYSO. The reported luminosities ($0.11 - 2.80 \times 10^{-6} L_{\odot}$) of the water masers were found to be in the circumstellar region of the MYSOs where water masers are found to have a luminosity in the order of $10^{-6} L_{\odot}$ (Lo, 2005). In addition,

multiple emission peaks were observed in the objects. The multiple water maser spots suggest the likely presence of several water masers not spatially co-located caused by the collision of the water masers and the jet around the core of the forming MYSO. On the other hand, NH_3 (2,2) in *G345.4938+01.4677* was detected mapping out the cold dense region of the emission.

Abbreviations

k_B	Boltzmann's constant
k_BT	Thermal energy
AMBER	Astronomical Multi-BEam combineR
ALMA	Atacama Large Millimeter/Submillimeter Array
AGN	Active Galactic Nuclei
AU	Astronomical Unit
ATCA	Australia Telescope Compact Array
CASA	The Common Astronomy Software Application
CRIRES	CRyogenic high-resolution InfraRed Echelle Spectrograph
FWHM	The full width at half maximum
FIR	Far-infrared
H_2	Molecular hydrogen
H II	H II region
HOPS	The H_2O Southern Galactic Plane Survey
IF	Intermediate Frequency
IRAS	Infrared Astronomical Satellite
IMF	Initial Mass Function
ISM	Interstellar Medium
ISAAC	Infrared Spectrometer And Array Camera
K-H	Kelvin-Helmholtz Timescale
$L_\odot$	Solar Luminosity
L_{Bol}	Bolometric Luminosity
MSX	Midcourse Space Experiment
MYSO	Massive Young Stellar Object
MIRIAD	Multichannel Image Reconstruction Image Analysis and Display

MIR	Mid-Infrared
MS	Main sequence
$M_{\odot}$	Solar mass
M_J	Jeans mass
NRAO	National Radio Astronomy Observatory
NIR	Near-Infrared
PPN	Proto-planetary nebulae
RFI	Radio frequency Interference
RMS	Red MSX Source (survey)
SED	Spectral Energy Distribution
SINFONI	Spectrograph for INtegral Field Observations in the Near Infrared
SNR	Singal-to-Noise Ratio
UCHII	Ultra-Compact H II region
UV	Ultra-Violet
VLA	Karl G. Jansky Very Large Array
VLT	Very Large Telescope
VLTI	Very Large Telescope Interferometer
V_{LSR}	Local Standard of Rest Velocity
YSO	Young Stellar Object

List of Figures

Contents

Chapter 1

Introduction

1.1 Background

Massive stars are thought to be responsible for most of the energetic feedback mechanism within our galaxies Urquhart *et al.* (2015), and they drive ionized jets during their formation prior to the stage where they form H II regions. It is thought that these are powered and collimated by magneto-hydrodynamic mechanisms associated with the accretion disc. This work seeks to examine the intricacies involved in massive star formation by studying emissions from water masers and ammonia (NH_3 (J,K) = (2,2), (3,3), (4,4), (5,5) and (6,6)) inversion transitions to investigate accretion disc and outflows in massive star forming regions. In order to further our understanding of how masers are pumped and moved away from the formation site, the accretion process, the timeline of the formation process and the direction of the disk and jets in massive star formation processes.

1.1.1 Stars

Stars are to the universe what cells (the smallest structural and functional unit of life) are to the human body. They are the fundamental units ("atoms") of luminous matter in the universe (Larson, 2003). They play a unique role in the processes and formation of our Galaxies, and are responsible, directly or indirectly, for most of what we see when we observe the observable universe (Larson, 2003). As such, it has become imperative to understand their formation processes. Over the years, significant progress has been made on both observational and theoretical fronts birthed by advancement in computational capacity and instrument resolution and sensitivity (interferometry) to understand various formation mechanism of stars. In spite of this progress, there is still no consensus on a generic predictive model that can be used to explain the underlying intricacies involved in formation of various (low, intermediate and high) mass stars that has gained wide spread acceptance by the astrophysical community for a given set of initial formation conditions. The differences in evolutionary sequence for low, intermediate and high mass stars is the likely reason for this. In the case of high-mass stars, they arrive at the main sequence still embedded in their natal cloud consequently prohibiting study of their earlier evolutionary stage while in low mass stars, their evolutionary sequence can be studied. Additionally, stars are formed in clusters of compact OB or large OB associations thus, making it difficult to differentiate between a single star and the cluster. There are two characteristic types of clusters, namely: globular and open clusters.

Globular clusters are made up of compact aggregation of thousands of stars (Krauss, 2000). They live in the halo of our galaxy and orbit the galactic centre suggesting they are formed early in the history of our galaxy. Studies of their spectra reveal the absence of heavy elements (carbon, oxygen and iron), suggesting the presence of primordial constituent elements (hydrogen and helium) in their clusters. Open clusters on the other hand, are relatively young (the youngest are just several million years old, while the oldest can reach a few billion years old Friel 1995) when compared with globular clusters. They live in the spiral arms of the galaxy and are very rich in heavy elements, suggesting they are formed in the latter stage of a galaxy's history.

1.1.2 Formation

Stars are formed in cold gas/dust (temperature $\sim$ 10 K), dense cores of molecular clouds. The formation process is triggered when the gravitational potential force overcomes the total internal pressure force in molecular clouds as shown in Figure 1.1. Radiation from massive stars, even when very young, exerts additional

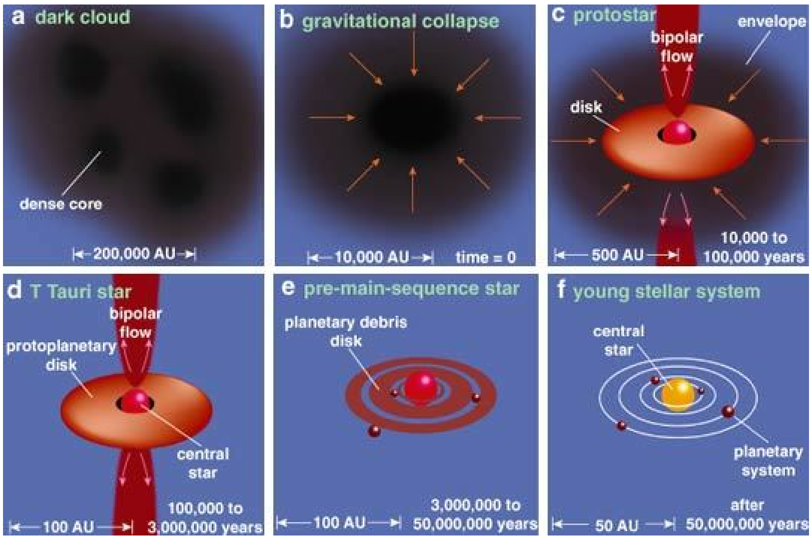

Figure 1.1: *Early development of a young, Sun-like star can be described in a series of stages that span more than 50 million years. Star formation begins inside dark interstellar clouds containing high-density regions (a) that become gravitationally unstable and collapse under their own weight (b). The collapsing core forms a protostar (c), a phase of stellar evolution defined by the rapid accumulation of mass from a circumstellar disk and a surrounding envelope of gas and dust. As the dusty envelope dissipates, the object becomes visible at optical wavelengths for the first time as a Tauri star (d). These objects can often be recognized in telescopic images by the presence of a protoplanetary disk (see Figure 5). After a few million years the dusty disk dissipates, leaving a bare pre-main-sequence star at its center (e). In some instances, a debris disk with newly formed planets may continue to orbit the star. The star continues its gravitational collapse to the point where its core temperature becomes hot enough for nuclear fusion, and the object becomes a main-sequence star (f). (AU = astronomical unit, the average distance between the Sun and the Earth (Greene, 2001)).*

pressure on the in-falling materials, and may overcome gravity to aid in the formation of such stars. The virial theorem governs the phenomena of a collapsing molecular cloud. For a self-gravitating system in equilibrium, the virial theorem states that

$$2U + \Omega = 0, \tag{1.1}$$

where Ω is the total gravitational potential energy of the cloud which is denoted,

$$\Omega = -\int_0^{M_c} \frac{GM(r)dM(r)}{r}, \tag{1.2}$$

and M_c is the total cloud mass with a shell of mass $dM(r)$ at radius r and G is the gravitational constant. The kinetic energy U from Equation (1.1) is defined as:

$$U = \frac{3}{2}nk_BT, \tag{1.3}$$

where k_B is the Boltzmann constant with uniform temperature T in Kelvin and n is the total number of particles.

Assuming a constant density, pressure and zero external (surface) pressure, Equation (1.2) is simplified to obtain

$$\Omega = -\frac{3}{5}\frac{GM_c^2}{R_c}, \tag{1.4}$$

where R_c is the radius of the cloud. The significances of Equation (1.1) for a cloud's stability are defined below:

- if $2U = -\ \Omega$, the cloud is stable;
- if $2U > -\ \Omega$, pressure wins: dispersion of cloud
- if $2U < -\ \Omega$, gravity dominates: there is contraction of cloud.

The third condition $2U < -\ \Omega$ implies that a cloud of radius R_c can condense if its mass exceeds the critical mass known as the Jeans' Mass (Jeans, 1902). From Equations (1.3) and (1.4) and assuming thermal pressure, the Jeans mass becomes:

$$M_J \simeq \left(\frac{5k_BT}{G\mu m_H}\right)^{\frac{3}{2}}\left(\frac{3}{4\pi\rho}\right)^{\frac{1}{2}}, \tag{1.5}$$

where μ is the mean molecular weight, m_H the mass of a hydrogen atom, ρ_c is the density of the cloud in kgm^{-3}. From Equation (1.5), M_J decreases with decreasing T and increasing ρ_c. For a typical dense core: $\rho_c \approx 10^{10}m^{-3}$, $\mu = 2.4$ and T $\approx$ 10 K, the Jeans Mass is computed as $M_J \approx 5M_\odot$.

Jeans' Length

Based on the virial theorem stated in Equation (1.1), we can estimate the typical length scale of a collapsing cloud. Assume the cloud has a volume V_c denoted by $\frac{4}{3}\pi R_c^3$, with a mass $M_c = \rho V_c$, where the density $\rho = \mu m_H n$ and pressure $P_c = nk_BT$. Using Equation (1.4) and solving for R_c we obtain

$$R_J \simeq \frac{1}{\mu m_H}\left(\frac{15k_BT}{4\pi Gn}\right)^{\frac{1}{2}}. \tag{1.6}$$

Free-fall Time

The Free-fall Time (t_{ff}) is the time-scale it takes for a pressure-free cloud to collapse dynamically to a very small size (nominally a point) under its own self-gravity; the time-scale depends on the average cloud gas density only. Using Equation (1.2) and ignoring pressure (because gravity dominates), the equation of motion for a thin shell with an initial radius, R_c, becomes

$$\frac{d^2r}{dt^2} = -\frac{GM(r)}{r^2} = \frac{4\pi GR_c^3\rho_c}{3r^2}. \tag{1.7}$$

Assuming that the acceleration is constant and the mass $M(r)$ internal to r also remains constant, it follows that

$$t_{ff} \simeq \sqrt{\frac{3}{2\pi G\rho_c}}. \tag{1.8}$$

The free fall time is independent of the initial radius of the cloud and $t_{ff} \propto \rho^{-\frac{1}{2}}$. The free fall time is longer for less dense regions and shorter for denser regions.

1.1.3 Massive Stars

Massive stars ($M \geq 8M_{\odot}$ and $10^3L_{\odot}$; Guzmán *et al.* 2016; Hosokawa & Omukai 2009; Mottram *et al.* 2011; Urquhart *et al.* 2015) evolve much faster than their low mass counterparts (Urquhart *et al.*, 2015). Massive stars have relatively short life spans with formation time-scales on the order of $\sim 10^5$ years when compared with their low mass ($M \leq 1M_{\odot}$) and intermediate mass ($M < 8M_{\odot}$) counterparts; implying that the star can reach the main sequence (MS) while still heavily embedded in its natal molecular cloud. They are formed in distant clusters (generally farther than 1kpc away) making it relatively challenging to observe when compared to low mass stars. Massive stars are also formed in compact OB clusters or large OB associations (Billington *et al.*, 2018). Thus, making it difficult to isolate single high-mass stars from its cluster, consequently limiting our ability to study them due to exacerbating source confusion.

Furthermore, massive stars are of significant importance in astrophysical processes such as: radiation, outflows, stellar winds, and supernovae explosions (Hosokawa & Omukai 2009; Urquhart *et al.* 2015). These astrophysical processes alter the interstellar/intergalactic medium through the destruction of a star's parent molecular cloud, thereby triggering further star formation within the star's immediate environment (Hennebelle & Commerçon 2014; Zinnecker & Yorke 2007). Further to this, studies by Urquhart *et al.* (2015) indicate that these activities enhance the chemical enrichment of the stars' environment. In addition, major sources of light from distant galactic sources are obtained from massive stars; and are used in the estimation of the cosmic formation rate (Hosokawa & Omukai, 2009).

Despite the importance and the unique role massive stars play in the energy budget, their formation processes are still not properly understood when compared to their low mass counterparts: whereby gravitational collapse of molecular cloud cores leads to matter accretion from a circumstellar disk, with the outward radiative force escaping via the poles and driving a fast bipolar wind (Davies *et al.* 2010; Hosokawa & Omukai 2009; see Figure 1.1c, d). Consequently, these aforementioned challenges about their formation and evolution have restricted our understanding and still remains an open and puzzling question that needs to be addressed (Hosokawa & Omukai 2009; Urquhart *et al.* 2015) .

The three different theories that have been put forward to explain the formation of massive stars are:

- massive star formation through the merging of less massive stars (coalescence);
- competitive accretion in a protocluster environment and
- gravitational collapse involving high-rate, disk-assisted accretion into the core which helps to overcome radiation pressure.

(See studies by Zinnecker & Yorke 2007 and Hennebelle & Commerçon 2014 for an in-depth review). Despite these theories, there is however little observational evidence to support the first model (Davies *et al.*, 2010), with a renewed interest in the later models. Recent studies by Kuiper & Yorke (2013) shows that the shielding of the disk by gas and dust at the surface of the accreting disk can lead to it surviving until a $100M_\odot$ mass star is formed.

1.1.4 Kelvin-Helmholtz Timescale

For a protostar to begin hydrogen burning and join the main sequence, it needs to contract further. The protostar can only achieve further contraction by radiating away the released gravitational energy. The timescale needed for the contraction to occur is called the Kelvin-Helmholtz timescale (hereafter K-H). This is the time it takes for a young stellar object (YSO) or stellar core to radiate its energy released during contraction. Typically, it takes 10^4 years for young high-mass stars but 10^7 years for solar-type stars (Dal Pino, 2005). Nuclear energy generation eventually offsets the energy loss caused by gravitational contraction (see review by Zinnecker & Yorke 2007). The timescale for contraction is given by:

$$t_{K-H} \sim \frac{\text{Gravitational Energy}}{\text{Luminosity}}.$$

$$t_{K-H} \sim \frac{GM^2}{RL}. \tag{1.9}$$

From the mass - luminosity relation, $L \propto M^\alpha$, where $2 < \alpha < 4$. Putting $\alpha = 4$ in Equation (1.9) we obtain

$$t_{K-H} \propto M^{-2}.$$

It follows from Equation (1.8) that

$$t_{ff} \propto \rho_c^{-\frac{1}{2}} \propto M^{-\frac{1}{2}},$$

therefore,

$$\frac{t_{K-H}}{t_{ff}} \propto \frac{1}{M^2} M^{\frac{1}{2}} = M^{-\frac{3}{2}}. \tag{1.10}$$

As the mass increases, the ratio $\left(\frac{t_{K-H}}{t_{ff}}\right)$ gets smaller and smaller implying that massive stars arrive on the main sequence while embedded in their molecular clouds (intermediate and massive stars arrive on the main sequence still accreting materials). Although low mass stars have an embedded pre-main sequence phase. High mass stars arrive on the main sequence still embedded, low mass stars do not. Thus, low mass stars have a visible pre-main sequence phase, whereas low high mass stars do not, they have an embedded pre-main sequence phase. How are they identified? In order to address this question, I will consider the mass accretion rate.

1.2 Accretion Disk and Jets

Accretion Disk

Accretion disks and outflows are a direct consequence of star formation (see Figure 1.1 for pictorial representation in the case of low mass stars and Figure 1.2 for a cartoon depicting accretion and jet phenomena). It is called an accretion disk because in addition to the conservation of angular momentum over a period of tens of thousands to millions of years, depending on the stellar mass, at the point where a disk is formed, the star is still in the process of being formed (i.e the star has not accreted all of its mass, hence, the protostar is still being fed with materials from the collapsing envelope). Theory predicts, and observations have been used to verify, that low mass stars (like the Sun) accrete the bulk of their mass through their circumstellar disks (Banerjee & Pudritz 2007; Beltrán *et al.* 2006). However, when it comes to high mass stars, the situation is still not known if massive stars also possess an accretion disk like their low mass counterparts, although several studies including work by Pudritz (1984) have predicted the presence of accretion disks in both low and high mass star forming regions.

Massive stars form so quickly: they have a short KH time scale ($t \sim 10^4 - 10^5$ years) and they spend the whole of their formation stages still embedded in a surrounding envelope. Additionally, they are at large distances (generally greater than 1kpc) and form in clusters (Beltrán *et al.* 2006; Beuther & Walsh 2007). Additional problems arises from the presence of energetic feedback mechanisms such as: radiation pressure, stellar winds and photoionization associated with massive stars. It is thought that these processes would ideally halt the vast amount of accretion required to form massive stars (Beltrán *et al.*, 2006).

However, according to Yorke & Sonnhalter (2002) and Beltrán *et al.* (2006), the aforementioned mechanisms can be avoided by the presence of a disk around massive protostars before massive stars are finally formed. Studies by Cesaroni *et al.* (2005) and Patel *et al.* (2005) indicates that the problem may be solved by non-spherical accretion which allows some of the stellar photons, radiative pressure, winds and hot ionized gas to escape along the axis perpendicular to the disk where the density is much lower. As a result, accretion disks are considered an essential element in the formation of low and high mass stars. An accretion disk has a size of $\sim$ 2000 AU in diameter (Davidson *et al.* 2011) is considered to be twice the centrifugal radius and geometrically thin (Adams *et al.*, 1987). Additionally, the orbital velocity of an accretion disk is close to Keplerian (Beuther & Walsh 2007; Kuiper *et al.* 2011) because the pressure gradient in the disk provides a distant (few thousand astronomical units) force that completely prevents it from orbiting Keplerian (Kuiper *et al.*, 2011).

Jets

Pudritz (1984) and (Bally, 2007) underscore the importance of astrophysical jets (Bipolar outflows) to the existence of accreting disk systems. According to Anglada *et al.* (2018) and Pudritz (1984), bipolar jets help to carry away prodigious amount of angular momentum and rotational energy away from the envelopes of an accreting disk. This enables more materials to accrete onto the central protostar. As a result, it sustains the star's formation process by enabling the star to accrete more mass from the surrounding material to form a type O or B star all other things being equal (Pudritz, 1984). Additionally, they generate turbulent motions, and can even disrupt the parent molecular cloud (Butcher *et al.*, 1980). Consequently, they represent a major channel in the self-regulation of stars' formation paradigm, and can also dominate feedback processes in regions where only low-mass stars are forming (Bally, 2007).

Although most protostellar jets observed are bipolar in nature, others are highly collimated, whereas others have wide-angle winds and a few are nearly isotropic and exhibit explosive behaviour (see Figure 1.3, Bally 2016). Factors including degree of collimation, flow orientation, mass-loss rate and velocity ejection (caused by morphologies and velocity field) all contribute to the variety of protostellar outflows. The velocity of these outflows ranges from a few km/s to over 10^3 km/s (Bally 2007, 2016). Jets have been observed to be usually located within 500 pc of a star's forming cloud and drive outflows with sizes ranging from hundreds of AU to tens of parsecs (Bally, 2007) with projected length between $\sim$ 0.01-1 pc. Recent work by Bally (2007) highlights the need for the study of jets. Through jets and outflows, histories of a forming star can be inferred by studying the fossil records of the mass loss. Additionally, they play a role in determining the final stellar masses and the shape of the Initial Mass Function (IMF) of the star. Also, jets alter the clouds chemical composition as they interact with molecules when ejected into their surrounding molecular environment. Jets and winds create cavities in the parent cloud, inject energy and momentum into the surrounding clouds, which in the absence of massive stars, may dominate the generation of turbulence and cloud motions.

Protostellar jets are responsible for a rich variety of phenomena in star forming regions, including maser emission, free-free, and synchrotron radiation at radio wavelengths, bipolar molecular outflows visible in tracers such as carbon-monoxide (CO) and many other molecules, shock-excited near-IR, visual, and UV radiation produced by a host of molecular, atomic, and ionized transitions, and in a few extreme cases, X-ray emission (Bally, 2007). The free-free emission from the ionized material very close to the young star makes the base of the jets bright at radio wavelengths (Butcher *et al.*, 1980). Direct observations of the evolutionary changes of jets can be studied due to their proximity, brightness and relatively short timescales (Krumholz *et al.*, 2004).

1.2.1 Radio Continuum

The quest to study and understand star formation and the interstellar medium (ISM) in the past and present at other wavelengths (optical, far, mid and near

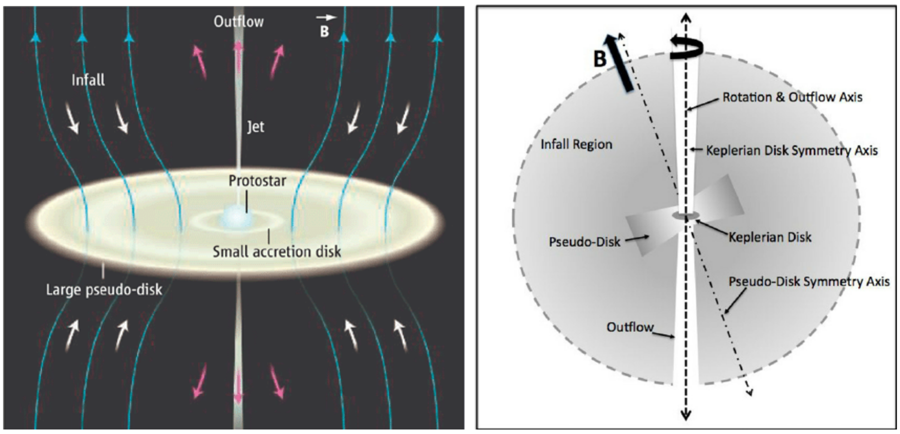

(a) (b)

Figure 1.2: *Summarizes the magnetically regulated core-collapse scenario. Typically, the diameter of the in-fall region is* $\sim 10,000\ AU$*, the diameter of a pseudo-disk is* $\sim 2000\ AU$*, and the diameter of a Keplerian disk is* $\sim 100\ AU$*. In the magnetically regulated core-collapse scenario: the pseudo-disk symmetry axis is aligned with the core magnetic field; and magnetic braking tends to align the core rotation axis with the magnetic field, but this alignment may not be exact. The pseudo-disk is a dynamically collapsing object formed by the magnetic fields, not rotation. The Keplerian disk is an object formed by rotation and so its symmetry axis is aligned with the cores rotation axis, as too is the outflow axis if the outflow is driven by rotation. (Davidson* et al.*, 2011).*

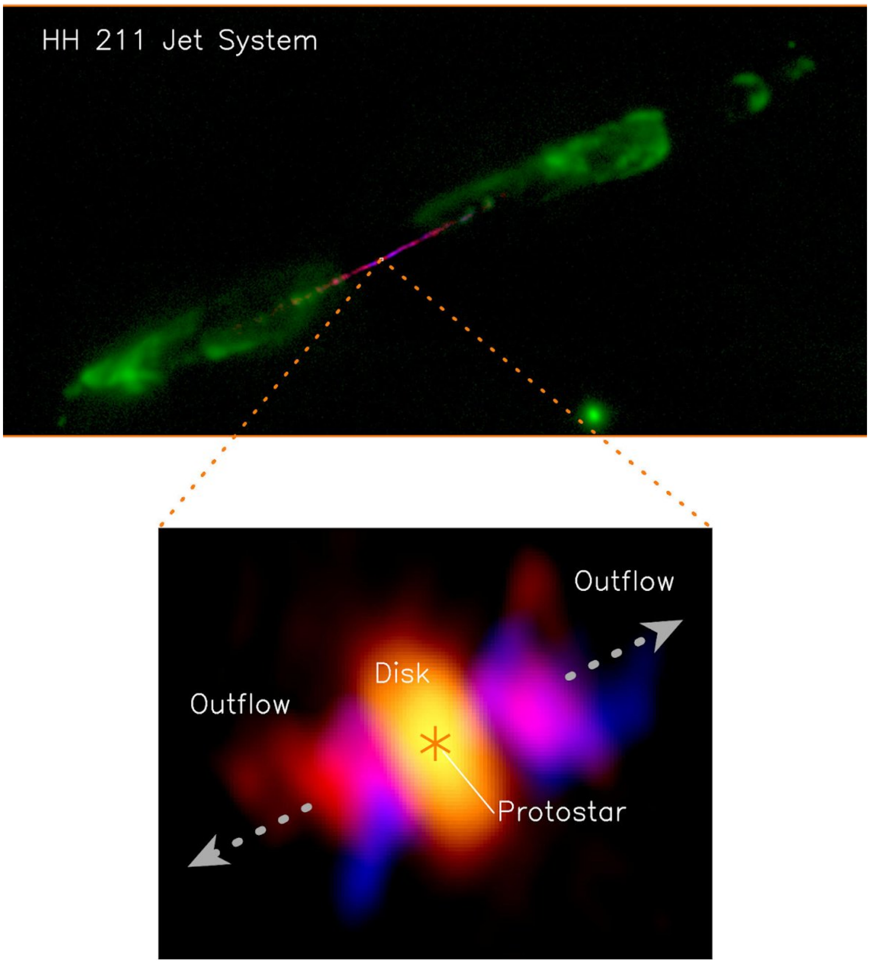

Figure 1.3: *Jet, disk, and outflow in the HH 211 protostellar system. (Top) A composite image showing the jet system. (Bottom) A zoom-in to the innermost region around the central protostar, showing the disk and outflow there. Asterisks mark the possible position of the central protostar. Gray arrows show the jet axis. Orange image shows the dusty disk at submillimeter wavelength obtained with ALMA. Blue and red images show the blueshifted and redshifted parts of the outflow coming out from the disk rotating around the jet axis. (*Lee et al., *2018).*

infra-red) has been extremely successful by aiding our understanding of galaxies and the universe. Although remarkable success has been achieved, there is still a huge desire to fully uncover and unravel unanswered questions (structures, composition and formation processes) that pertains to stars and the ISM at the finest possible resolution. Furthermore, various studies using advanced radio telescopes such as VLA, ATCA among others to study the ISM and MYSOs at radio wavelengths have been carried out and have been hugely successful: by improving our understanding of the formation and evolutionary processes of stars and galaxies. Observing at radio wavelengths is a desirable option because of its ability to penetrate the dense and optically thick dusty envelopes within which protostars are usually embedded Consortium *et al.* (2012) and Anglada *et al.* (2018) which was otherwise lacking at other wavelengths (optical/infrared as a result of short wavelengths obscured by dust). In addition, at radio wavelengths, accurate astronomical positions (parallax) of the interested science targets are obtained (Anglada *et al.* 2018; Rodriguez 1997). It can also be used to determine the direction of the jets. The free-free emission at cm wavelengths can be used to estimate important physical properties of MYSOs as previously established by Anglada *et al.* (2018) and Bally (2016).

Centimetre continuum emission from young protostars, for example, the low mass T Tauri pre-main sequence stars, are dominated by free-free emission from their thermal jets (Cohen *et al.*, 1982). According to Anglada *et al.* (1996), these objects also emit a small fraction of non-thermal emission that gains prominence at their later stages of evolution. A similar case is expected in high mass stars if their formation mechanisms are similar. A property that will be used, if identified, to distinguish between younger and more evolved MYSOs. Some of the quantities of interest that can be derived from radio sources include radio spectral flux densities and angular sizes. Once these quantities are extracted, other quantities such as physical sizes, jet opening angle and kinematic ages can also be established. In addition to the listed quantities above, spectral indices of the objects can also be estimated if their flux densities at other frequencies are available in the literature e.g Curiel *et al.* (2006).

1.3 Molecular Tracers

Spectra of molecules in (YSOs) jets display emission lines and continuum radiation and have been detected in all bands of the electromagnetic spectrum.

The spectral lines allow measurements of radial velocities and physical parameters such as density, temperature, and pressure over a wide range of conditions (Bally, 2007). The problem of identifying a reliable massive disk tracer prohibited statistical studies of larger disk samples in the past (Beuther & Walsh, 2007). This work hopes to use ammonia tracer and water maser emission to study the kinematics of disks around massive star forming regions to help shed more light on our understanding the dynamics involved in massive star formation processes.

1.3.1 Ammonia as a Diagnostic

Ao *et al.* (2011) underscore the importance of molecular gas as a means for harnessing information about gas densities, temperatures, and kinematics within Galaxies. In 1968, Cheung *et al.* (1968) detected interstellar ammonia (NH_3): the first interstellar polyatomic molecule discovered through microwave emission. Since its discovery, it has proven to be a valuable spectroscopic tool in the study of the interstellar medium (ISM) and has the ability to detect a wide range of excitation conditions due to its ubiquitous nature (Ho & Townes, 1983).

Molecules such as carbon monoxide (CO), carbon sulphide (CS), hydrogen cyanide (HCN), and formyl cation (CHO^+) are other commonly observed species in the interstellar medium. These molecules have been successfully used in the past to map the ISM and massive star forming regions, depending on the science goal, as seen in the works of Fleck Jr (1988), Leung & Brown (1977) and Gao & Solomon (2004). In addition, CO effectively maps areas of lower density (e.g. clouds, Gao & Solomon 2004). It is however unable to effectively study very-small scale structures and highly excited regions of the ISM due to the lack of singular sensitivity to either density or temperature, consequently making it difficult to resolve structures within such molecular regions (Ao *et al.*, 2011).

Ammonia presents us with another window to effectively characterize all types of regions containing molecular materials within the interstellar medium. In addition, important properties such as the presence of metastable and non-metastable states, ortho, (J,K)= $(0, 3, 6, 9, ...)$ and para, (J,K)= $(1, 2, 4, 5, 7, 8, ...)$ species, inversion and hyperfine structures makes ammonia of particular interest in astrophysical conditions (Ho & Townes, 1983). The ubiquitous nature of ammonia

(J,K)	Rest Frequencies (MHz)	Energy (K)
NH_3(2,2)	23722.633	64.90
NH_3(3,3)	23870.129	124.50
NH_3(4,4)	24139.4169	200.52
NH_3(5,5)	24532.9887	295.37
NH_3(6,6)	25056.025	412.40
H_2O maser	22235.080	-

Table 1.1: *A table showing water maser with its rest frequency along with ammonia transitions with their corresponding rest frequencies and upper-energy levels. Energy levels for NH_3(2,2), NH_3(3,3) and NH_3(6,6) were taken from Ho & Townes (1983) and NH_3(4,4) and NH_3(5,5) were retrieved from Wong et al. (2018).*

makes it an excellent tracer of regions of active low and high mass star formation. Also, its inversion lines are quite close in frequency, thus allowing us to measure sources with similar beam size. The hyperfine components of ammonia enable us to estimate the optical depth of the transition. In addition, the presence of different transitional ladders in ammonia allow us to deduce recent conditions of the ISM. According to Ho & Townes (1983), the ratio between the rotational temperature of ortho and para ammonia species can be used to reflect conditions at earlier times and rotational temperature between similar species to reflect recent conditions.

The use of ammonia $(2, 2)$ through $(6, 6)$ transitions will therefore allow us to trace gas on a wide range of scales and temperatures around massive young stellar objects. The high excitation temperatures ($T > 20$ K) will ensure that we are not tracing cold gas envelopes (Beuther & Walsh, 2007). Table 1.1 gives the line transitions, rest frequencies and upper energy level of the NH_3 transitions for the targets.

1.3.2 Water Maser

Factors such as distance to the formation site, embedded nature (due to short Kelvin Helmholtz time scale) and the rarity of massive young stellar objects has prohibited the clear distinction between MYSOs and their low mass counterparts. In the light of these limiting factors, astronomers are constantly looking for novel tools and techniques to enable them to distinguish between low and high mass formation processes. In addition to the aforementioned factors, occurrence of other features such as the presence of circumstellar discs, collimated outflows and jet rotation makes it challenging to delineate the formation processes of MYSOs from their low mass counterparts due to similarities in their formation paradigm. Through the use of astronomical masers, uncovering the driving mechanism of outflows in MYSOs is therefore an accessible point of comparison between high-mass and low-mass star formation.

During the formation of MYSO, water masers are formed near the core as a result of collisional pumping. A maser is an acronym for microwave amplification by stimulated emission of radiation. As a result, water masers serve as point-like tracers of a star forming region and three-dimensional velocity field (when there is multiple maser spots) of the environment in which they lie (Castangia *et al.*, 2017). Water maser species are excited in strong shocks on a working surface between a protostellar outflow and a dense envelope. Through the study of water masers, we are able determine the mass lost rate in MYSOs and in addition, inherent features of an outflow in close proximity (a few hundred AU, Goddi *et al.* 2005) within the formation site. Using Equation 1.11 (Reynolds 1986), the mass loss rate is determined by:

$$\dot{M}_{Jet} = \frac{9.38 \times 10^{-6} v_8 \mu S_{mJy}^{\frac{3}{4}} d_{kpc}^{\frac{3}{2}} \theta_{OA}^{\frac{3}{4}}}{x_\circ \nu_{10}^{\alpha} \nu_{m10}^{(0.45-\frac{3\alpha}{4})} T_4^{0.075} (\sin i)^{\frac{1}{4}} F^{\frac{3}{4}}}, \tag{1.11}$$

where α is the derived spectral index, μ is the average particle mass (as a fraction of the proton mass), x_0 is the ionisation fraction, ν_8 is the terminal velocity of the jet (assumed to be 500 km s^{-1} from proper motion studies in literature), S_ν is the integrated flux density, d is the distance to the source, ν_{m10} is the turnover frequency, i is the inclination angle (assumed to be $\sim 39°$), T is the electron temperature, θ_{OA} (Equation 1.12 from Purser 2017) is the opening angle at the base of the jet and F is defined in Equation 1.13

$$\theta_{OA} = 2 \tan^{-1} \left(\frac{\theta_{min}}{\theta_{maj}} \right), \tag{1.12}$$

$$F \equiv F(q_\tau, \alpha) \equiv \frac{4.41}{q_\tau(\alpha - 2)(\alpha + 0.1)}, \tag{1.13}$$

and

$$q_\tau = \frac{2.1(1 + \in + q_T)}{\alpha - 2}, \tag{1.14}$$

where q_τ is the power-law coefficient with which the opacity falls with distance along the jet propagation axis, q_T is the equivalent of q_τ for temperature, $\in$ is the equivalent of q_τ for jet width and α is the spectral index. Furthermore, outflow properties such as (size, velocity, and morphology) differ with sources (Burns *et al.*, 2016). Stellar mass, evolutionary stage, geometry of the surrounding envelope, and the driving mechanism of host outflows are likely cause of the observed variations (Motogi *et al.*, 2016).

1.4 Problem Statement and Objective

Massive stars arrive on the main sequence still embedded in their natal cloud due to their short ($\sim 10^4$ years) Kelvin-Helmholtz time scale. As a result, it is challenging to study the changes they undergo from their formation to the stage where they form H II regions (An H II region is a region of interstellar atomic hydrogen that is ionized). The surface temperature within such a region is in the order of T $\sim 10^5$ K). In addition, it is widely believed that massive stars have accretion disks and outflows associated with them just like their low mass counterparts (Purser *et al.*, 2017). The accretion disk helps to drive ionized jets during their formation prior to the stage where the H II region is formed. These astrophysical activities are believed to be powered and collimated by magneto-hydrodynamic mechanisms associated with the accretion disk. A previous study by Betz & McLaren (1980) revealed the presence of ammonia in the circumstellar envelopes of a star forming region. Hence, we seek to:

- use ammonia as a diagnostic tool to resolve the disk (look for changes in the size of the disk) thereby studying the structure, composition and evolution of the star in order to look for patterns and correlations that will offer clues to how the jets vary with mass and age;

- The properties of the radio jets (luminosities, mass loss rates, morphology) will be compared with measures of the stellar mass and age,
- Use water masers to infer the presence of star forming activities and how the offset of the water maser relates to the jet of the object.

In addition to the use of ammonia molecular tracer, radio continuum results (images) will be processed and vital information such as image size, radio spectral flux densities, peak flux and angular dimensions will be extracted and compared with the work of Purser (2017).

1.5 Thesis Outline

The organisation of this thesis is as follows: the precursory Chapter gives a framework of the research: background, problem statement, aim and structure of the research. Chapter 2 presents an overview of the Australia Telescope Compact Array, the science targets, calibrators used, data reduction and imaging processes are outlined and discussed. The subsequent Chapter 3, highlights the main part of the work where the results on the continuum of our various science targets are presented. Chapter 4 is a continuation of the results which highlight the result of the spectral line emission. This section will focus on ammonia and water maser emission. The final and concluding chapter, Chapter 5, contains the discussion and analysis of the results by comparing with previous work carried out on similar sources. Finally, we conclude the work with possible further recommendations made where suitable.

Chapter 2

Observations and Data Reduction

2.1 Target Selection

The observed five MYSOs were all selected from the Red MSX Source (RMS) surveys (Lumsden *et al.*, 2013). The RMS survey has identified ~ 3000 MYSOs and H II region candidates located throughout the Galactic plane. The sources were initially identified from their mid-infrared colours using the MSX point source catalogue and Two Micron All Sky Survey (2MASS) colour selected sources. The five MYSOs selected for the study satisfy luminosity $L_{bol} > 20000 L_{\odot}$, declination $\delta \leqslant -40^{\circ}$ and distance d $\leqslant$ 4 kpc. The declination limit was set to target sources that are too far south to be accessible with the Very Large Array (VLA). In addition, all sources apart from G345.4938+01.4677 were previously known to have detected NH_3 (2,2) emission from the Mopra data (see `http://rms.leeds.ac.uk/cgi-bin/public/RMS_CONE_SEARCH.cgi` for details). This is a complete set of the most luminous nearby MYSOs. Table 2.1 lists the science targets at 22.24 to 24.5 GHz observing frequency using ATCA observed from 9^{th} to 12^{th} October, 2014.

2.2 The Australian Telescope Compact Array

The Australian Telescope Compact Array (hereafter ATCA) is a radio interferometer consisting of six 22 m dishes, creating 15 baselines in a single configuration.

Object	RA (J2000)	Dec. (J2000)	Distance (kpc)	$L_{Bol}(L_{\odot})$
G310.0135+00.3892	$13^h51^m37^s.85$	-61°39'07".5	3.20	6.70×10^4
G332.9868-00.4871	$16^h20^m37^s.81$	-50°43'49".81	3.60	1.80×10^4
G339.8838-01.2588	$16^h52^m04^s.66$	-46°08'33".6	2.70	6.40×10^4
G345.4938+01.4677	$16^h59^m41^s.61$	-40°03'43".3	2.40	1.50×10^5
G345.5043+00.3480	$17^h04^m22^s.87$	-40°44'23".5	2.00	1.00×10^5

Table 2.1: *A table of the target sources, their positions, distances and bolometric luminosities adopted from the Red MSX Source (RMS) survey (Lumsden* et al.*, 2013).*

It is sited at latitude 30° and longitude 149°. While five antennas (CA01 to CA05) are movable along a 3 km long east-west track and a 214-m long north-south spur (see Figure 2.1), allowing the creation of hybrid arrays, one antenna (CA06) is fixed at a distance of 3 km from the western end of the track. Each antenna has a set of six cryogenically cooled low noise receivers sampling the frequency range from 1.1 to 105 GHz (i.e. wavelengths from 3 mm to 30 cm), apart from CA06 which does not have a 3 mm receiver system (Wilson *et al.*, 2011).

Figure 2.1: *The Australia Telescope Compact Array (ATCA), located at the Paul Wild Observatory near Narrabri, approximately 550 km north-west of Sydney. Displayed are five of the six 22-m cassegrain antennas, here arranged in one of the hybrid configurations which include two antennas on the North-South Spur. (Wilson* et al.*, 2011).*

2.3 Observational Set-Up

Observations were made using the ATCA over the period of four days between October 9th to 12th 2014 under the project code C2935. For the purpose of our science goal, observations were conducted in 1.5 km baseline configuration mode. The selected MYSOs fall within a distance range of 2 - 3 kpc with an effective beam of ∼ 8000 AU (∼ 25.8 arcsec), at a range of $22.235 - 25.044$ GHz observing frequencies. In this mode, the cooler (T $\leqslant$ 100 K) regions will be fully resolved.

SpwID	# Chans	Frame	Ch0(MHz)	ChanWid(kHz)	TotBW (kHz)	CtrFreq(MHz)	(J,K)
0	33	TOPO	23924.000	-64000.000	2048000.0	22900.0000	-
1	33	TOPO	25524.000	-64000.000	2048000.0	24500.0000	-
2	3073	TOPO	22292.000	-31.250	96000.0	22244.0000	H_2O
3	2049	TOPO	23892.000	-31.250	64000.0	23860.0000	NH_3(3,3)
4	2049	TOPO	24180.000	-31.250	64000.0	24148.0000	NH_3(4,4)
5	2049	TOPO	24564.000	-31.250	64000.0	24532.0000	NH_3(5,5)
6	2049	TOPO	25076.000	-31.250	64000.0	25044.0000	NH_3(6,6)
7	2049	TOPO	23764.000	-31.250	64000.0	23732.0000	NH_3(2,2)

Table 2.2: *A table representing the continuum channels (SpwID 0 and 1) and line channels in SpwID 2 to 7. The water maser is located in SpwID 3. All other SpwID below 3 represents the various ammonia inversion transitions considered for the study.*

Table 2.2 gives a summary for day ones' observation and Table 2.3 gives summaries for the remaining three days observations (10th to 12th September, 2019). The first two spectral windows identification (SpwID) in Table 2.2 and 2.3 represent the continuum. The remaining SpwIDs represent the lines with SpwID 2 in Table 2.2 representing the water maser. All other SpwIDs in both Tables 2.2 and 2.3 represent various ammonia inversion transitions. The Water maser was targeted on the first day of the observation only (see Table 2.2). Antenna CA04 was used as the reference antenna for the observations. In addition to the observed science object, data for four other objects known as calibrators were also taken to aid in the calibrations of flux and phase of the science targets (see Table 2.4) and Figure 2.2 shows a typical uv-coverage for the science object G310.0135+00.3892 during an observation on the 9th of October, 2014. Figure

SpwID	# Chans	Frame	Ch0(MHz)	ChanWid(kHz)	TotBW (kHz)	CtrFreq(MHz)	Rest Frq. (MHz)
0	2049	TOPO	23924.000	-1000.000	2048000.0	22900.0000	-
1	33	TOPO	25524.000	-64000.000	2048000.0	24500.0000	-
2	2049	TOPO	23892.000	-31.250	64000.0	23860.0000	23870.129
3	2049	TOPO	24180.000	-31.250	64000.0	24148.0000	24139.4169
4	2049	TOPO	24564.000	-31.250	64000.0	24532.0000	24532.9887
5	2049	TOPO	25076.000	-31.250	64000.0	25044.0000	25056.025
6	3073	TOPO	23764.000	-31.250	96000.0	23716.0000	23722.633

Table 2.3: *A table representing the continuum channels (SpwID 0 and 1) and line channels i.e. SpwID 2 to 6. The line channels represents the various ammonia transitions considered for the study. The rest frequencies column corresponds with the different ammonia inversion transition ladders (J,K) in Table 2.2. The rest frequency of the H_2O maser used in the clean process is 22235.080 MHz.*

2.2 gives an idea of the coverage of the sources during observation. The gap in the uv coverage determines the quality of the final image. From Figure 2.2, the position of the antenna with respect to the source and inadequate integration time $\sim$ 2.5 hours (i.e. time spent in observing the the object) affect beam of the array by elongating the beam. This generates side lobes in the final image and a poor signal to noise ratio (SNR). On the other hand, a well represented uv-coverage results in circular beam shape and less side lobes with better SNR.

2.4 Calibrators Used and Data Reduction

The data was edited, calibrated, and imaged in the standard fashion using the Common Astronomy Software Application (hereafter CASA: McMullin *et al.* 2007) package instead of the traditional ATCA software reduction package Miriad (Sault *et al.* 2011). The flux, phase and bandpass calibrators and their properties are listed in Table 2.4.

The recorded synthesis visibility data were in RPFITS. As a result, the task *importatca* was used to convert the dataset into measurement set (e.g .ms file). In radio interferometry, the frequencies that are observed are also used by various terrestrial devices (microwave ovens, commercial FM radio and TV stations,

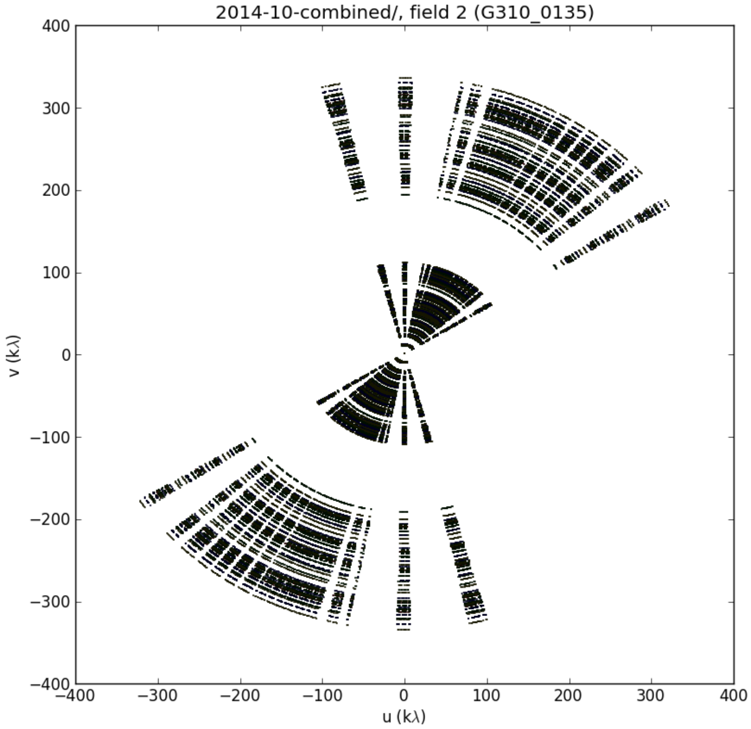

Figure 2.2: *Plot of the sampling function (single channel at 24.5 GHz) for the 2014 data towards G310.0135+003892. The plot shows the radial uv-plane coverage over the 64 MHz bandwidth (1.5 km baseline) obtained with the ATCA telescope.*

cellphones, digital satellite TV's) whose radio emission leak into the recorded visibilities. This is aided by the fact that an antenna is not just sensitive to the science target in which it is pointing to but as well as objects in the region of the survey. As such, flagging (about 8 percent of data was flagged) and inspection was done using CASA task commands. In addition, the fluxes for the phase visibility data was scaled up using the flux calibrator. The flux calibrator 1934-638 does not have a standard flux density model in CASA. Consequently, the flux model was manually computed using Equation 2.1. The model was proposed by Partridge *et al.* (2016) for frequencies above 11 GHz. The *setjy* task was then

Calibrators	RA (J200)	Dec. (J200)	Type	S_ν (Jy)	Science Targets
1921-293	$19^h24^m51^s.06$	-29°14’30”.1	Bandpass	8.59 ± 0.11	
1934-638	$19^h39^m25^s.03$	-63°42’45”.6	flux	0.85 ± 0.156	
1352-63	$13^h55^m46^s.63$	-63°26’42”.6	phase	0.732 ± 0.01	G310.0135
1646-50	$16^h50^m16^s.65$	-50°44’48”.4	phase	1.277 ± 0.01	G332.9868, G339.8838
1646-50			phase	1.277 ± 0.01	G345.5043, G345.8838

Table 2.4: *A table of positions, calibration types and fluxes for the calibrators used the reduction of the data. In the final column, the science target(s) listed are the sources to which the complex gain solutions are transferred to, from the relevant calibrator (first column).*

used to scaled up the fluxes.

$$\log S = 5.8870 - 1.3763 \log \nu. \tag{2.1}$$

A plot of flux density versus frequency for the phase calibrators used was also made to check the accuracy of *setjy* model made using Equation 2.1 (see Figure 2.3). Also, from Equation 2.1, S is the flux density in Jy and ν is the frequency in MHz.

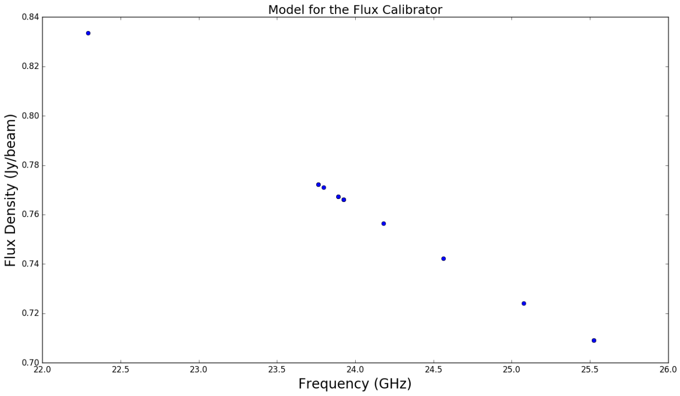

Figure 2.3: *A graphical representation of the scaled flux calibrator*

After computation of the flux density model, an initial phase calibration was carried out to account for the small variations of phase with time in the bandpass. Furthermore, the bandpass calibration was done by first solving for the delay calibration. This is an important step because it solves for the relative delays of each antenna relative to the reference antenna, after which the bandpass calibration was performed on the data to account for gain variations with frequency. Furthermore, we perform the gain calibration between our various sources and the phase calibrators to minimize the effect of atmospheric conditions. Other than bandpass calibration, phase and flux calibration solutions were also calculated and applied to the bandpass calibrator. The solutions were finally applied to other calibrators as well as the science targets using the task *applycal*. The phase calibrator solutions were then split and cleaned to check the accuracy of the calibration process. The images appeared as point source as expected (see Figure 2.4).

2.4.1 Imaging

Continuum

The cleaning of the data was carried out in two stages: multi-frequency synthesis (mfs) mode for the continuum channels and velocity mode for the spectral line channels. During cleaning of the continuum images, a cell size of ~ 0.44. This was obtained by dividing the resolution for the synthesis beam by 5. The image size of 298 arcsec was used in imaging. For ATCA, the image size is obtained by $\frac{1.06\times\lambda}{D}$, where D is the diameter of one ATCA telescope and λ is the wavelength (observing frequency). In addition, Briggs weighting (Briggs, 1995) with robustness of $\sim$ 0.5 was adopted during imaging. Natural and uniform weighting were avoided because the former increases side-lobes which adds noise to science targets that are usually faint and the latter spreads noise around the science targets. Hence, the decision to use Briggs weighting: a weighting whose image resolution lies between natural and uniform weighting. The synthesized beam is 2 arcsec and the primary beam is 149 arcsec.

Spectral Line

On the other hand, when cleaning the other spectral windows (i.e. those containing the spectral lines and water maser), a different approach was adopted. The 'velocity' spectral gridding mode was used. In addition, other clean parameters such as start, width, number of channels (nchan) and local standard of rest

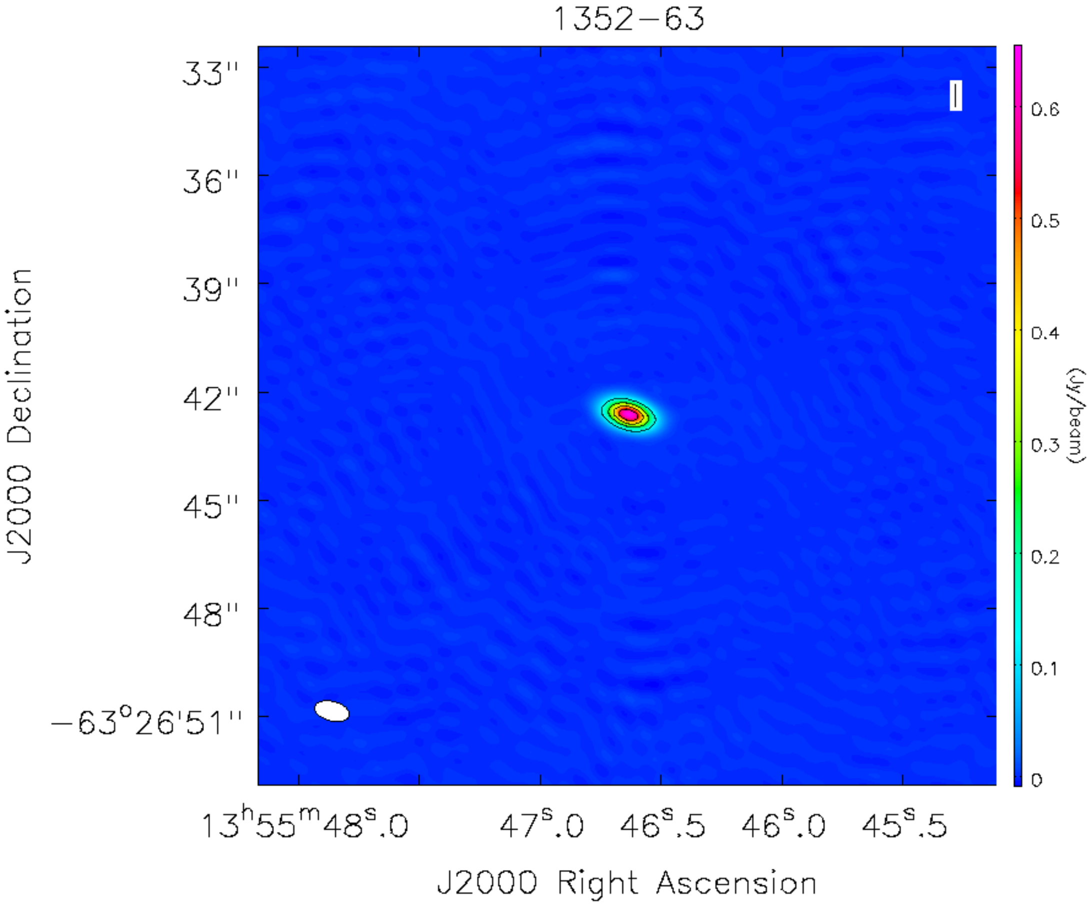

Figure 2.4: *Model for* 1352−53 *phase calibrator depicting as a point source object.*

velocity were all used in the clean process. The spectral resolution in the zoom band with the 64 MHz configuration is 0.4 km s^{-1}. Also, the velocities relative to the local standard of rest (v$_{lsr}$) for the science targets are listed in Table 2.5. The threshold for the flux level to stop cleaning was set to 0.01 mJy using the

Object	v_{lsr} km/s	Start (km/s)	Width (km/s)	#chan
G310.0135+00.3892	-39.700	-462.750	0.395	1200
G332.9868-00.4871	-56.400	-478.030	0.422	1200
G339.8838-01.2588	-32.000	-347.87	0.421	1200
G345.4938+01.4677	-12.600	-433.96	0.421	1200
G345.5043+00.3480	-17.000	-253.00	0.421	1200

Table 2.5: *A table of the target sources with their velocity relative to the local standard of rest obtained from RMS survey, (Lumsden et al., 2013).*

Briggs weighting.

The theoretical thermal noise level of (73 - 106 μJy/beam) was determined using Equation 2.2 below:

$$S_{rms} = \frac{\sqrt{2} k_B T_s W}{10^{-26} A_{ant} \varepsilon \sqrt{N_{ant}(N_{ant}-1)\Delta v \tau}}, \tag{2.2}$$

where S_{rms} is the RMS noise level, k_B is Boltzmann's constant in units of $J.K^{-1}$, T_s is system temperature, A_{ant} is the surface area in a single antenna in units of m^2, N_{ant} is the number of antennas in the array, Δv is the bandwidth, in units of MHz, and τ and ε are the integration time, in units of seconds and the efficiency of the antenna (where for a perfect antenna $\varepsilon = 1$) respectively. Also, W is the image weighting factor (where for Natural weighting W=1).

2.4.2 Doppler Tracking

The ATCA like other radio interferometry e.g Very Large Array (hereafter VLA) does not Doppler track. This is because it is impractical for telescopes like ATCA and VLA to predict phase jumps resulting from frequency changes between successive scans. VLA however does Doppler setting. Doppler setting is a method of calculating the sky frequencies of all the lines resources at the start of an observation and keeping the frequencies fixed for that resources for the entire duration of the observation. It will account for large doppler shift $\sim$ 30 km/s caused by the Earth's orbit around the Sun and Solar motion (van Moorsel, 2014).

The frequency ν at which we must observe a spectral line is derived from the rest frequency of the spectral line ν_0, the line of sight of velocity of the source

(V), and the speed of light (c). The true line of sight velocity, is related to the observed and rest frequencies by

$$V = \frac{v_0^2 - v^2}{v_0^2 + v^2} c. \tag{2.3}$$

The Equation 2.3 is simplified in astronomy to the two different approximations mostly used:

- Optical velocity

$$V^{optical} = \frac{\lambda - \lambda_0}{\lambda_0} c = cz, \tag{2.4}$$

where z is the redshift of the source.

- Radio velocity

$$V^{radio} = \frac{v_0 - v}{v_0} c = \frac{\lambda - \lambda_0}{\lambda} c \neq V^{optical}. \tag{2.5}$$

The radio and optical velocities defined in Equations 2.4 and 2.5 are not identical. Particularly, the V^{optical} and V^{radio} diverge at large velocities. The optical is dominated by (Barycentric) extragalactic observations and local standard of rest (hereafter LSR) radio velocities are typical for galactic observations as discussed below. Doppler tracking is where the sky frequency for the observation is calculated and adjusted at the start of every individual scan during subsequent observations. Because ATCA does not Doppler track and correct for the systemic velocity of a source, the observer has to enter the actual sky frequency of the spectral line of interest. In converting to sky frequency, the observing frequency has to consider

- The known systemic velocity of the source. There are two conventions in use for defining the velocity used: the radio and optical conventions. There are also two commonly used rest frames: the solary system barycentre, and LSR. There are two classes of LSR: the kinematics LSR (LSRK) and the dynamic (LSRD) which represent the kinematics and the dynamic centres, respectively. In most cases, LSRK is being used.

Because of the Earth's motion, the frequency that corresponds to a particular velocity of an astronomical source will change with time. When observing spectral lines, many observatories continuously change the observing frequency to account for the effect of the Earth motion, and thus make a particular source velocity correspond to a single channel. Although the spectral lines occur at a well defined frequencies, the lines do have a non-zero widths. The width is calculated using Equation 2.6.

$$\frac{\triangle f}{f} \simeq \frac{\triangle \nu}{c}, \tag{2.6}$$

where $\triangle f$ is the bandwidth (Hz), f the rest frequency (Hz), $\triangle \nu$ is the velocity span (channel width (Hz/beam)) and $c = 3 \times 10^5$ km s^{-1}, the speed of light. The start values for each spectral windows for the different water and ammonia spectral lines were computed using the v_{lsr} values from Table 2.5 and the equation in Equation 2.7.

$$v_{lsr} = nchan \times \left(\frac{1}{2} \triangle \nu\right) + start, \tag{2.7}$$

where start, v_{lsr} and channel width have their usual units in km s^{-1}.

Chapter 3

Continuum Emission

3.1 Introduction

The results of four science targets (sources) are discussed in this chapter with their corresponding spectral energy distributions (SEDs) diagrams and parameters in Table 3.1. From the five MYSOs observed, only four were detected in our studies. The source G345.5043+00.3480, was not detected possibly because it was too extended. The target G345.5043+00.3480 has previously been detected as seen in papers by Lumsden *et al.* (2013), Yu & Wang (2014), and Purser (2017).

Additionally, extensive radio studies on the science targets have been carried out by Purser *et al.* (2016) using the ATCA at 5.5, 9, 17 and 22.8 GHz frequencies. The resolution of the synthesised beams are 2.25, 1.38, 0.73 and 0.54 arcseconds respectively. This corresponds to a maximum baseline length of 6 km. At 24.5 GHz observing frequency in the 1.5 km array set-up mode, a resolution of 2 arcseconds is achieved. The resolution is comparable to the 9 GHz and higher frequency (17 and 22.8 GHz) bands to compare structures. As a result, we seek to compare the structures of the targets at both frequencies. In addition, the fluxes obtained from our studies are compared with the fluxes from the paper of Purser *et al.* (2016) at 22.8 GHz.

3.2 Fluxes and Spectral Indices measurement.

The parameters for the various science targets were obtained using the CASA task *imfit*. The task works by fitting one or several Gaussian profiles to the object. The parameters of the fit gives an estimate of the properties (e.g. fluxes, density, position angles, major and minor full width at half-maximum (hereafter $FWHM$) of the objects. The deconvolved dimensions (size of the objects) were obtained using Equation 3.1

$$\theta_{Actual} = \sqrt{\theta_i^2 - \theta_{Beam}^2}, \tag{3.1}$$

where θ_{Actual}, θ_i and θ_{Beam} represents the actual size (deconvolved size) of the source, the observed $FWHM$ of the source and the $FWHM$ of the restoring beam respectively.

Error measurement of the spectral indices for each of the sources was performed using least square fitting algorithms. Error values on the fluxes for the sources were obtained using a 1D Gaussian fitting including a generally acceptable absolute 10 percent flux calibration error. The fluxes at 5.5, 9, 17 and 22.8 GHz were extrapolated from the thesis of Purser (2017), and the errors on the fluxes for each source were computed using the square root of the sum of the squares of the errors by Dobaczewski *et al.* (2014) in Equation 3.2

$$\delta E = \sqrt{(\delta E_1)^2 + (\delta E_2)^2 + (\delta E_3)^2 + \cdots + (\delta E_n)^2}, \tag{3.2}$$

where δE is the error, $\delta E_1, \delta E_2, \delta E_3$ are the errors on each flux for the various components (core, lobe, jet) of the object and δE represents the total number of flux present in each object.

3.3 G310.0135+00.3892

The source is associated to the IRAS object 13481-6124. A total integration time of 2.5 hours was used in observing the source. The object has a mass of $\sim 20 M_\odot$ and is of spectral type O9 class. Fedriani, R. *et al.* (2018) determined the age of the object as $\sim 6 \times 10^4$ years. Other properties derived from the RMS survey by Lumsden *et al.* (2013) for the object are listed in Table 2.1 and 2.5. In addition, previous work by Purser *et al.* (2016) using the ATCA at 1.32 cm wavelength determined the mass-loss rate of the object to be $\sim 1.8 \times 10^{-5} M_{\odot}$ yr^{-1} and momentum rate in the range of $\sim 1 - 2 \times 10^{-2} M_{\odot}$ yr^{-1} km s^{-1}.

Previous studies by Ilee *et al.* (2013) observed the presence of strong emission from the image of the source. The observed emission is attributed to be emanating from the carbon monoxide (CO) within the region where the source is located. The study (observation of the source) by Ilee *et al.* (2013) was carried out using the Very Large Telescope (VLT) at 2.3 μm wavelength achieving a spatial resolution of $\sim$ 0.316 arcseconds. From our work (see Figure 3.1, contours in magenta colour), the image has a bandwidth of 64 MHz, a beam size of 1.29×0.42 arcsec ($\sim$ 4128 × 1344) AU and signal to noise ratio (SNR) of 46.66. The sensitivity of the source was estimated as 0.46 mJy/beam. A compact, bright central component (see point label S in Figure 3.1) is observed with additional two distinct components (lobes) in the west (W) and South-West (SW) respectively. The lobe observed in the SW is consistent with the findings of Purser (2017) and Kraus *et al.* (2010) (see emission with white contours in Figure 3.1). However, the component labelled W is reported for the first time.

Purser *et al.* (2016) used the ATCA at 9 GHz observing frequency with 6 km configuration set-up and Kraus *et al.* (2010) used the Very Large Telescope Interferometry (VLTI) to study the source between June 2008 and May 2009 within at a wavelengths range of 1.95 - 2.55 μm having a 130 m maximum baseline configuration with corresponding resolution range of 0.0037 - 0.0043 arcseconds. The inner environment of IRAS13481-6124 reveals a compact elongated structure as reported by (Kraus *et al.*, 2010).

In addition, when a 1D Gaussian was fitted to the emission in Figure 3.1, a flux density of 1.53 ± 0.08 mJy/beam was observed. Purser *et al.* (2016) reported a flux density of 1.89 ± 0.16 mJy/beam at 22.8 GHz in 6 km baseline configuration mode. The slight variation in the fluxes is likely due to the differences in the different array configuration adopted during the observation of the source at 9 and 24.5 GHz respectively. The gaps in the uv coverage is another likely reason for the low flux recovery. Kraus *et al.* (2010) reported a position angle of 114° for the source.

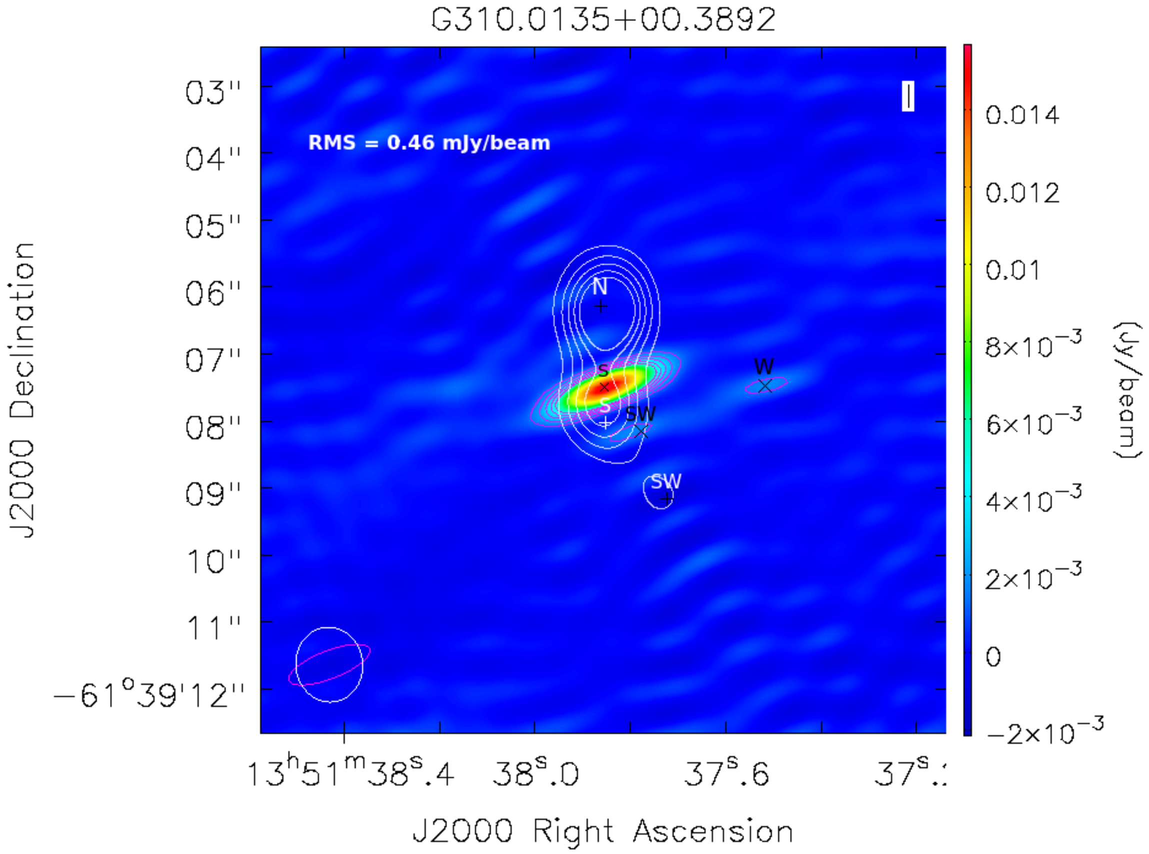

Figure 3.1: *ATCA maps of the radio continuum emission from the G310.0135+00.3892 at 9 (contoured in white) and 24.5 GHz (contoured in magenta). The image at 9 GHz was obtained from the data of (*Purser et al., 2016*). Beams are shown in the lower left corner of the panel. The contour intervals are at -3, 3, 5, 7, 9 and 11 times σ (1σ = 0.46 mJy/beam).*

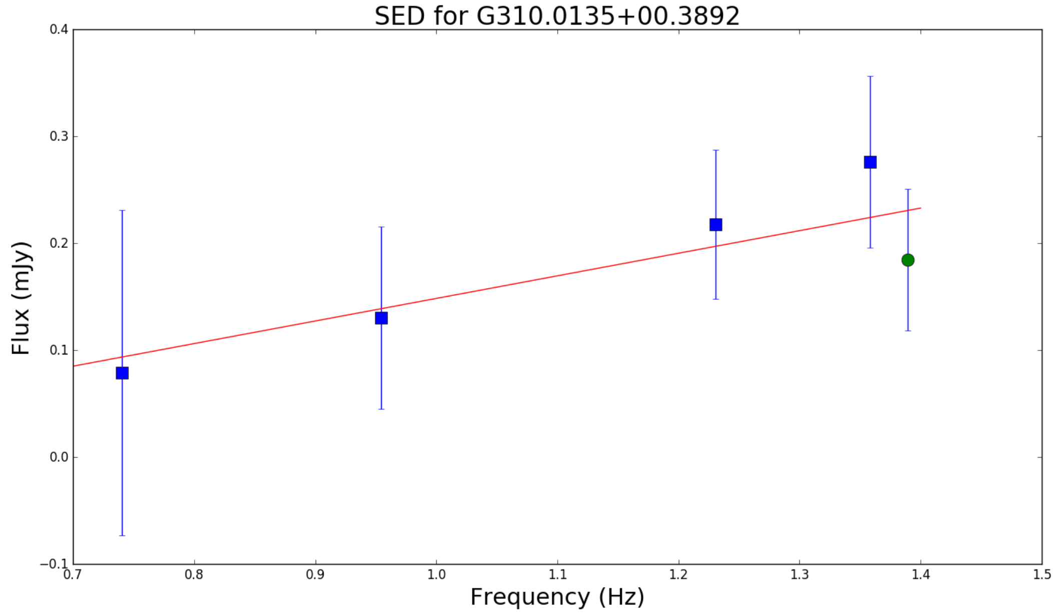

Figure 3.2: *Plotted SED for the target source G310.0135+00.3892 recovered from the Gaussian fitting. The best fit to the measured fluxes is shown in red line. Error bars on the recovered fluxes include a 10 percent absolute flux-scale uncertainty expected from observation using the ATCA. The point with green circle represents data from our study.*

In a recent studies by Purser *et al.* (2016), the object was unresolved at lower frequencies (5 and 9 GHz) due to signal to noise ratio and small spatial scales involve in recovering the deconvolved sizes. However, at 17 GHz, the south component was determined to have a size of of 0.17 ± 0.03 arcsecond (544 AU). From the 1D Gaussian fitted to the emission, the object was (only marginally) resolved in one direction with an upper limit of ($\sim$ 4128 × 1344) AU. Also, at 1.5 km configuration mode and 24.5 GHz observing frequency, it was expected that more structures will be observed. This however was not achieved due to low sensitivity when compared with the sensitivity of 42.3 μ Jy/beam achieved by Purser (2017). This gives a low ($\sim$ 47) to high signal ($\sim$ 50 Purser 2017) noise ratios. As a result, most structures were not revealed. In addition, the Figure in 3.2 represents the SED plot for the object (the point with green circle mark represents data from our study) and the spectral index is listed in Table 3.1. The plot follows a power law distribution and has a spectral index of 0.21 ± 0.19. The positive spectral index of the target indicates the presence of free-free emission. Purser *et al.* (2016) however inferred that the object is an ionised jet displaying both thermal and non thermal emissions.

3.4 G332.9868 - 00.4871

The source was observed with a total integration time of 2.5 hours. Properties of the source obtained from the RMS survey Lumsden *et al.* (2013) can be found in Tables 2.1 and 2.5. Ilee *et al.* (2013) observed the presence of carbon monoxide in G332.9868-00.4871. The carbon monoxide emission is attributed to coming from the presence of an accretion disk around the central source (see label C in Figure 3.3).

Studies by both Wheelwright *et al.* (2012) and Purser (2017) found the object to exhibit a spherically symmetrical and a compact morphology. In addition, Purser (2017) fitted a homogeneous H II region model to the source and reported an emission measure of $1.17 \pm 0.14 \times 10^9$ pc cm^{-3} with a size of $\sim$ 300 AU and a spectral index of $\alpha = 1.27 \pm 0.14$ for G332.9868-00.4871. Furthermore, at 5, 7, and 9 GHz, the object was not resolved due its compact morphology reported by Wheelwright *et al.* (2012) and (Purser, 2017).

From our studies at 24.5 GHz, the image of the source has a sensitivity of 0.259 mJy/beam, SNR of 17.42 and a beam size of 1.07 × 0.54 arcsec (3852 × 1944) AU. When a 1D Gaussian was fitted to Figure 3.3, the object was resolved with a size of 3.05 × 0.69 arcsec (10980 × 2484) AU. In addition, from our studies, a flux density of 12.92 ± 0.59 mJy/beam was obtained when compared to 10.48 ± 0.5 mJy/beam obtained by (Purser, 2017). Table 3.1 shows the properties of the target obtained using a 1D Gaussian fitting.

From Figure 3.3, at 24.5 GHz, we report an elongated structure in the Nort-Southh East (NSE) and North-South West (NSW) directions with a bright central compact component (label C) and a bulged component in the west (Label W) directions. Additionally, we report a slightly thin east component (label E) when

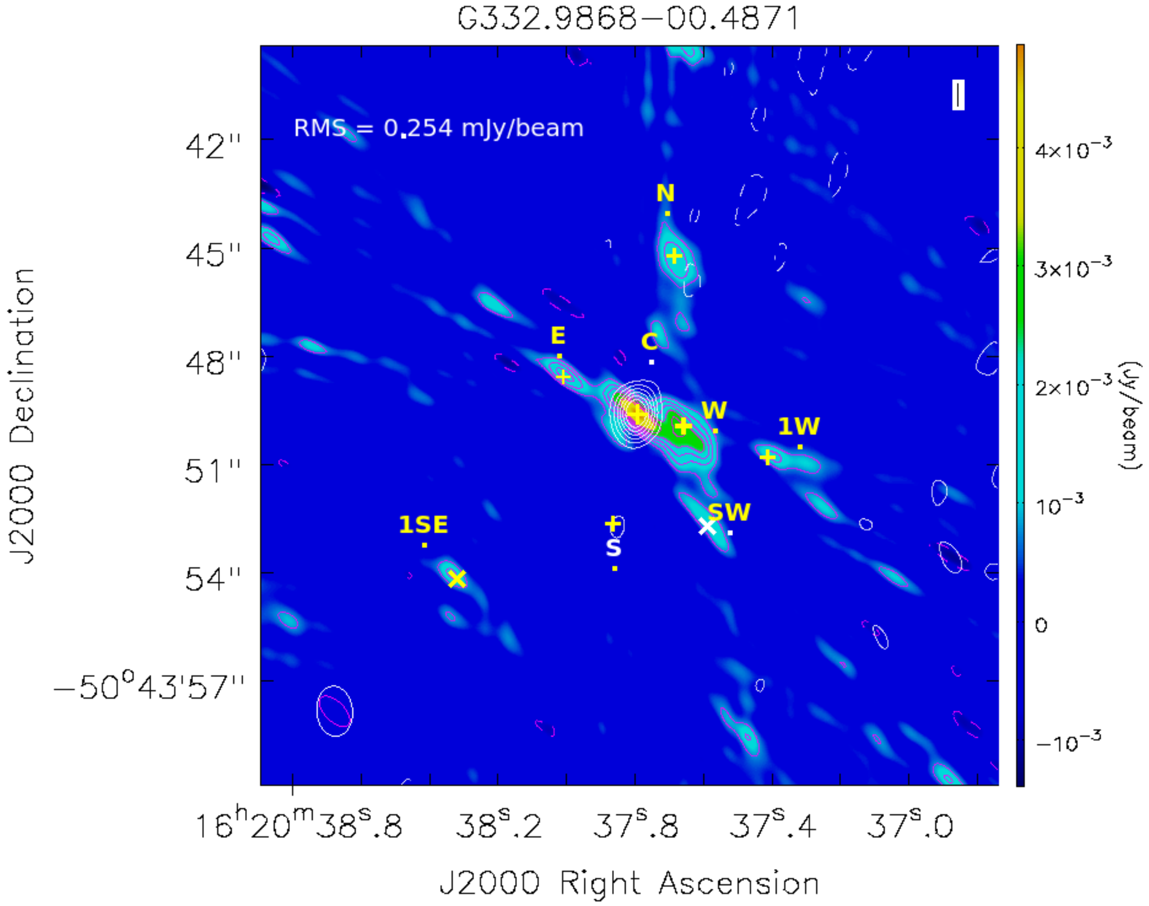

Figure 3.3: *ATCA maps of the radio continuum emission from G332.9868 - 00.4871 at 9 (contours lines in white) and 24.5 (contours in magenta) GHz. The image at 9 GHz was obtained from the data of (Purser et al., 2016). Beams are shown in the lower left corner of the panel. The contour intervals are at -3, 3, 5, 7, 9, 11 and 13 times σ (1σ = 0.254 mJy/beam).*

compared with the west component. Other structures are observed in the north (label N), far west (label 1W), far south east (label 1SE) and south west (see label SW) directions. The central (label C) and south (label S) structures were the only structures previously reported by Purser (2017) at 9 GHz (see image in Figure 3.3 with white contours). Although we observed more structures when compared with Purser (2017) at 9 GHz, we report a low sensitivity of 0.259 mJy/beam compared with 155 μJy/beam reported by (Purser, 2017). We infer the presence of a bipolar jet for the observed structure in Figure 3.3. This observation is consistent with the findings of (Purser, 2017). A spectral index of $\alpha = 1.26 \pm 0.14$ obtained from our studies is in close agreement with the findings of (Purser, 2017). The positive spectral index follows a power law distribution and indicates the likely presence of free free emission in the source. The Figure in 3.4 represents the SED plot for the source and Table 3.1 has other parameters obtained using Gaussian fitting.

3.5 G339.8838-01.2588

The object is associated to the IRAS object 16483-4603. The source like the previous sources was observed for a period of 2.5 hours. In a study by Purser *et al.* (2017), the object was estimated to have a spectral index of $\alpha = 0.77 \pm 0.04$ and inferred to have the nature of a conical, thermal jet undergoing some degree of acceleration. In addition, due to the turn-off at higher frequencies, the authors inferred the presence of a young, optically thick ultra compact H II region. The object is said to have class B V spectral type (Ellingsen *et al.*, 1996).

In studies by Ellingsen *et al.* (1996), G339.8838-01.2588 is attributed to be a strong site for methanol maser emission at 6.7 and 12.2 GHz with linear spatial distribution. The presence of methanol maser activity has also been reported by De Buizer *et al.* (2002). In addition to this, De Buizer *et al.* (2002) found the object to have an elongated structure with ionised emission. Furthermore, it was found that the emission from the radio continuum originates from two sources within the same surroundings. De Buizer *et al.* (2002) inferred that the two sources are relatively close to each other. The first of the two emissions from the likely sources emanates from an unshaded massive star with an extended

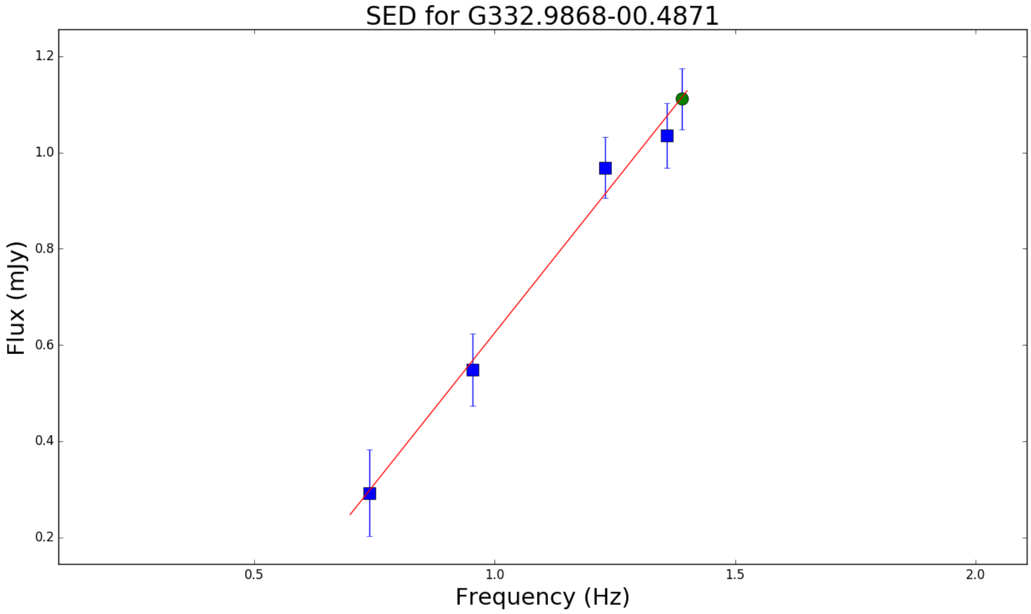

Figure 3.4: *Plotted SED for the target source G332.9868-00.4871 recovered from the Gaussian fitting. The best fit to the measured fluxes is shown in red line. Error bars on the recovered fluxes include a 10 percent absolute flux-scale uncertainty expected from observation using the ATCA. The point with green circle represents data from our study.*

H II region. It is thought that the emission is responsible for the observed radio continuum emission with the outflow coming from the central region.

From our work, the image of the source has a sensitivity of 0.105 mJy/beam with a SNR of 28.29. The image has a beam size of 1.09 × 0.54 arcsec (2943 × 1458) AU. From Figure 3.5, an extended structure is observed with a bright compact central morphology with lobes in the NE and SW direction at a position angle of 45.64 degrees. The result is consistent with results from the studies of Purser *et al.* (2017), where all three lobes were observed at all four (5, 9, 17 and 24.5 GHz) observing frequencies. When a 1D Gaussian was fitted to the emission, the size (deconvolved) component has a major and minor axes of 4.84 × 0.73 arcsec (13068 × 1971) AU.

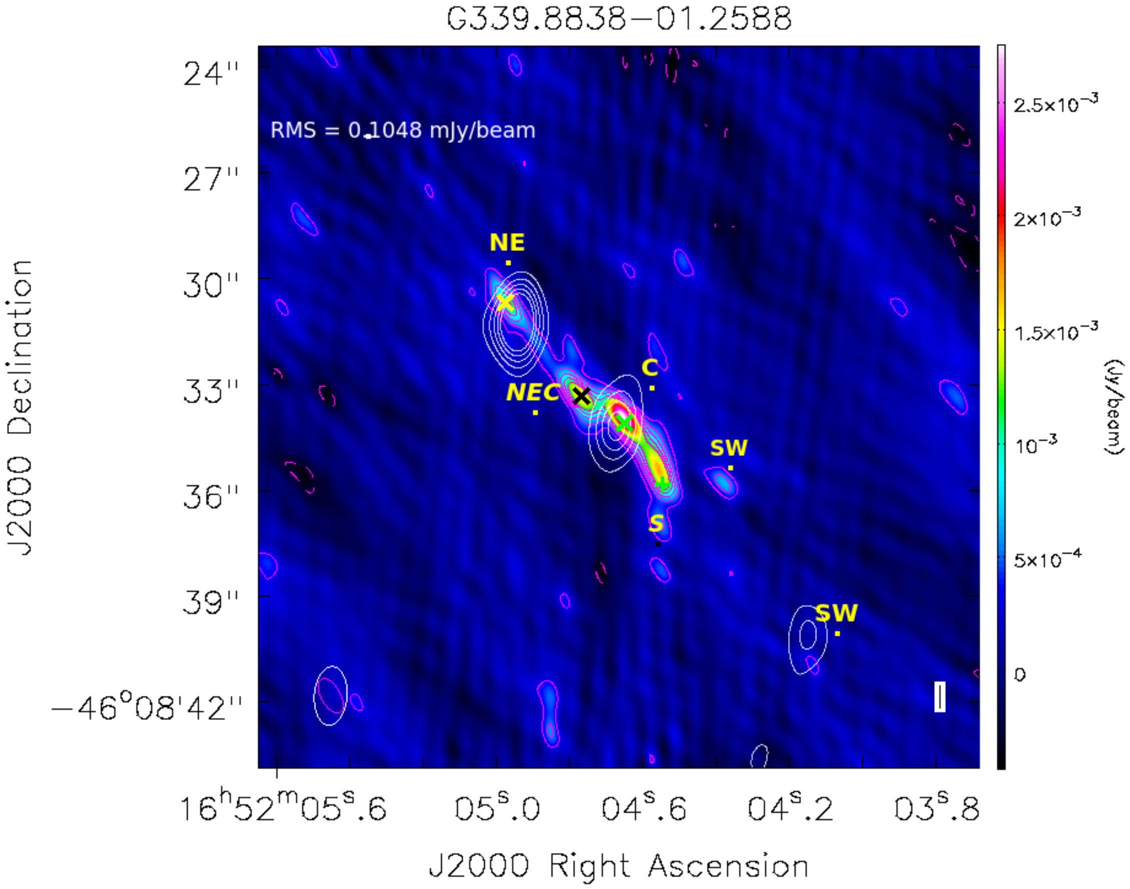

Figure 3.5: *ATCA maps of the radio continuum emission from G339.8838-01.2588 at 9 (contours lines in white) and 24.5 (contours in magenta) GHz. The image at 9 GHz was obtained from the data of (*Purser et al., 2016*). Beams are shown in the lower left corner of the panel. The contour intervals are at -3, 3, 5, 7, 9 and 11 times* σ *(*$1\sigma = 0.1048$ *mJy/beam).*

In addition, the *FWHM* for the object is $\sim 1.36 \pm 0.11$ arcseconds. A flux density of 4.59 ± 0.96 mJy/beam was obtained from our work. The result is in close agreement with the findings of (Purser *et al.*, 2017). The difference in the arrays is the likely reason for the variation. Although more structures were observed at 1.5 km array configuration mode when compared with Purser (2017) at 6 km configuration mode, the low sensitivity of 0.105 mJy/beam compared with the sensitivity level of 62.1 μJy/beam reported by (Purser, 2017) may have prohibited finest structures being resolved. At all five frequencies, the object was fully deconvolved. Figure in 3.6 is the SED plot of the object with a negative spectral index (see Table 3.1). A spectral index, $\alpha = -0.0 \pm\ 0.11$ was obtained from our findings. This value is consistent with an H II region and in agreement with the report of Ellingsen *et al.* (1996).

3.6 G345.4938+01.4677

G345.4938+01.4677 (also known as IRAS 16532-3959). The source has been extensively studied using the ATCA at four frequencies (1.4, 2.4, 4.8 and 8.6 GHz, Guzman *et al.* (2010) and (5.5, 9.0, 17.0 and 22.8 GHz) by Purser *et al.* (2017). The source is located at 1.6 kpc (Guzman *et al.*, 2010). It has a gas mass of $\sim 900 M_\odot$ and the central mass of the star is estimated as $\sim 15 M_\odot$ (Guzmán *et al.*, 2014). The source is reported to have a dense molecular core (9×10^5 cm^{-3}, Guzmán *et al.* (2011)). Other properties (position, v_{lsr}, and bolometric luminosity) of the source are listed in Tables 2.1 and 2.5.

Previous studies by Guzman *et al.* (2010) reported the detection of a compact, bright central component consisting of four outer lobes. The authors argue that the continuum emission from the central object corresponds to a free-free emission from the jet, whereas the emission from the outer lobes corresponds to thermal emission arising from the interaction between the shocks and the surrounding medium. Follow up studies by Guzmán *et al.* (2011), Guzmán *et al.* (2014), Guzmán *et al.* (2016) and Csengeri, T. *et al.* (2018) presents findings consistent with the work of Guzman *et al.* (2010). Additionally, the compact, bright central component reported by Guzman *et al.* (2010) at 1.4, 2.4 and 4.4 GHz was resolved in two separate lobes (I-E and I-W) at 8.6 GHz. The findings of Purser *et al.*

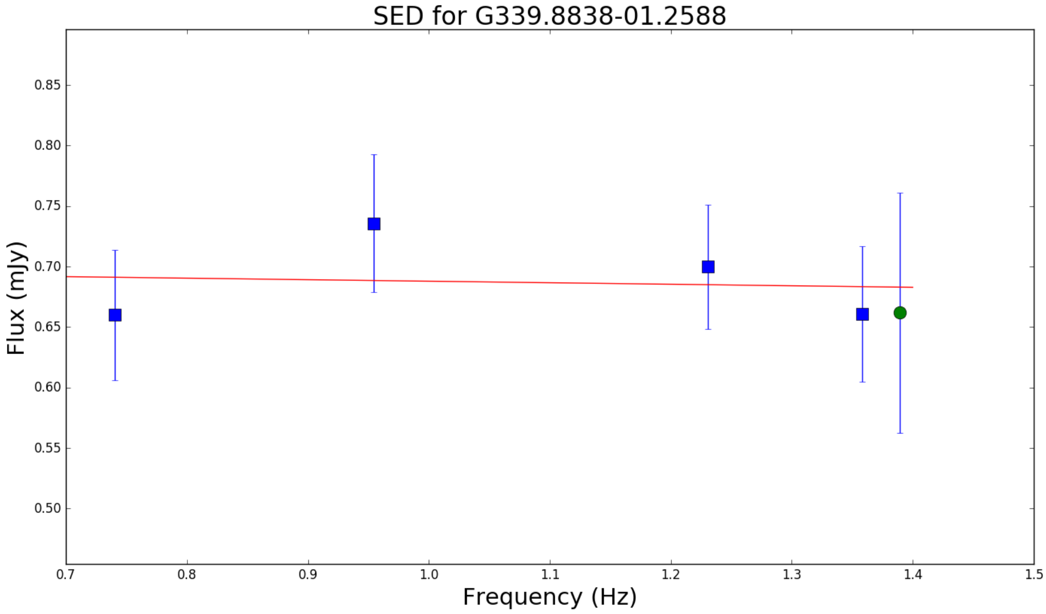

Figure 3.6: *Plotted SED for the target source G339.8838 - 01.2588 recovered from the Gaussian fitting. The best fit to the measured fluxes is shown in red line. Error bars on the recovered fluxes include a 10 percent absolute flux-scale uncertainty expected from observation using the ATCA. The point with green circle represents data from our study.*

(2017) at 17 GHz is in agreement with this observation. In addition, Purser *et al.* (2017) reported a spectral index $\alpha = 0.85 \pm 0.15$ for the compact central component. The result further solidifies the result by Guzman *et al.* (2010).

At 24.5 GHz, the beam size of the image of the source is 1.86×0.58 arcsec (2616×1392) AU, sensitivity of 0.581 mJy/beam and SNR of 21.15. From Figure 3.7, a bright central compact component (label C) is observed with distinct outer lobes in the west (label 1W) and east (label 1E). The central component and the distinct out lobes in the east and west have been previously reported by Guzman *et al.* (2010) Guzmán *et al.* (2014), Guzmán *et al.* (2016) and Purser *et al.* (2017). Although the bright central component was observed in our work, most components (lobes) reported by the aforementioned authors at various frequencies

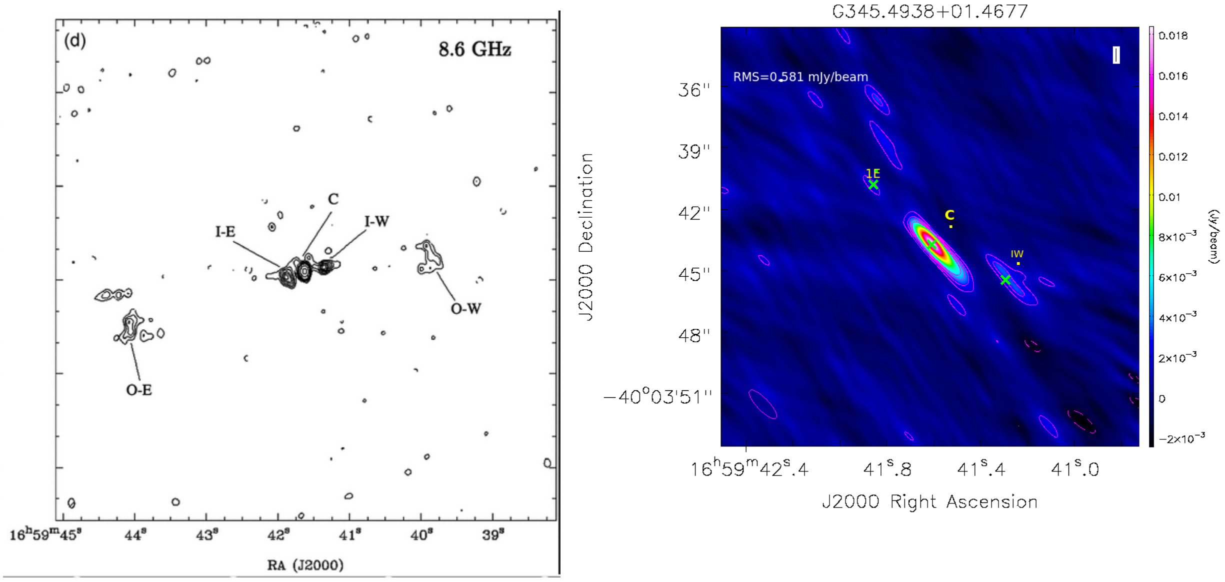

(a) (b)

Figure 3.7: *ATCA maps of the radio continuum emission from G345.4938+01.4677 at 9 and 24.5 GHz. The ATCA radio continuum emission map at 9 GHz was obtained from* Guzman et al. (*2010*)*. Beams are located on the bottom left corner of each panels. The contour levels at 9 GHz are -4, 3, 6, 9, 13, 16, 19, 24, 50, and 100 times* σ *(1*σ *= 0.081 my/beam). The contour levels at 24.5 GHz are -3, 3, 5, 7, 9 and 11 times* σ *(1*σ *= 0.581 mJy/beam)*

were not detected due to a higher noise 0.58 mJy/beam level from our studies compared to 140 μJy/beam reported by (Purser, 2017) and 0.081 mJy/beam reported by Guzman *et al.* (2010). The lobe (O-W) detected by Guzman *et al.* (2010) was not detected. A spectral index of $\sim 0.83 \pm 1.72$ was recorded by Purser *et al.* (2017). A flux density of $S_\nu \sim 23.88 \pm 0.96$ mJy/beam is observed. This value is in close agreement with a value of $S_\nu \sim 21.71 \pm 0.88$ mJy/beam reported by Guzman *et al.* (2010) and Purser *et al.* (2017). When a 1D Gaussian was fitted to the emission, the deconvolved size of 2.015×0.215 arcsec (4836×516) AU is obtained at a position angle of $\theta_{PA} = 40.18$ degrees. The SED plot is shown in Figure 3.8. The SED has a positive spectral index of 0.34±0.45, suggesting the presence of free free emission. Other properties obtained using Gaussian fitting is reported in Table 3.1.

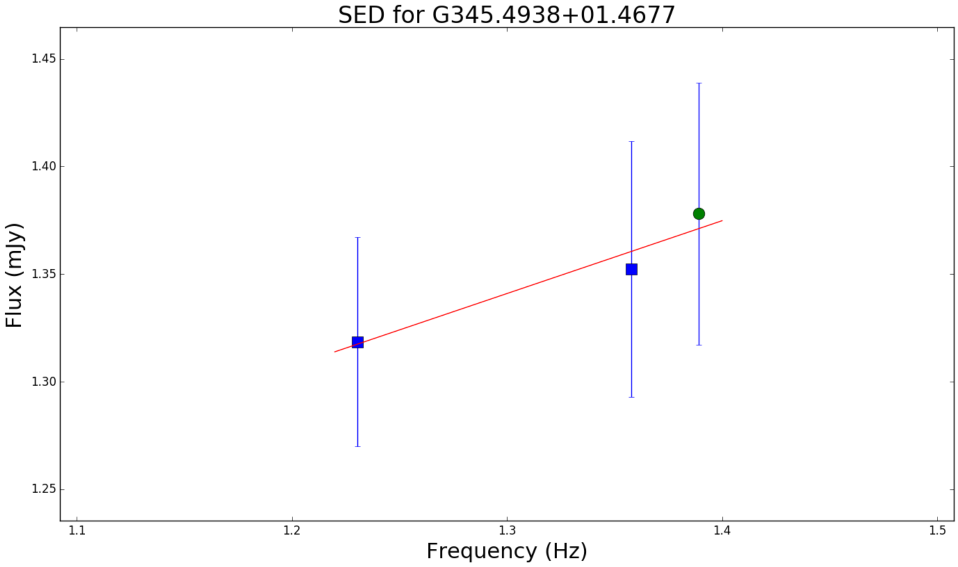

Figure 3.8: *Plotted SED for the target source G345.4938+01.4677 recovered from the Gaussian fitting. The best fit to the measured fluxes is shown in red line. Error bars on the recovered fluxes include a 10 percent absolute flux-scale uncertainty expected from observation using the ATCA. The point with green circular represents data from our study.*

Source	S_ν^a (mJy)	S_ν^b(mJy)	RMS (mJy beam^{-1})	SNR	α^a	α^b
G310.0135+00	1.53±0.08	1.89±0.16	0.46	46.66	0.21±0.19	1.80±1.67
G332.9868-00	12.92±0.59	10.48±0.59	0.26	17.42	1.26±0.14	1.27±0.14
G339.8838-01	4.59±0.59	4.58±0.13	0.10	28.29	-0.01±0.11	-0.34±0.14
G345.4938+01	23.88±0.96	21.6±0.83	0.58	21.15	0.34±0.45	0.83±1.72
G345.5043+00	-	0.08±0.01	0.63	2.82	-	1.78±0.89

Table 3.1: *Target sources observed with ATCA between 09/10/2014 and 12/10/2014. The table shows their observed fluxes, sensitivity (RMS), spectral indices, signal to noise ratio (SNR) when fitted with 1D Gaussian to their emission. The fluxes in column one (i.e. S_ν^a) is the observed fluxes from our studies at 24.5 GHz and the fluxes in column two (i.e. S_ν^b) were taken from Purser's thesis Purser (2017) at 22.8 GHz. The column with label α^a represents the spectral index obtained from the SED plot in Figure 3.2 and α^b from Purser (2017).*

Source	Beam (")		Deconvolved (")		Position Angle $\theta_{P.A}$(°)	
	major axis	minor axis	maj. axis	minor axis	Beam	Decon.
G310	1.29	0.42	1.29	0.42	-68.72	-68.72
G332	1.07	0.54	3.05±0.30	0.69±0.08	44.67	63.90±1.90
G339	1.09	0.54	4.84±0.41	0.73±0.07	29.32	45.64±0.94
G345	1.86	0.58	2.02±0.19	0.22±0.04	43.67	40.18±0.94
G345.5	6.05	0.78	29.45±3.49	4.92±0.51	32.48	37.9±1.50

Table 3.2: *Table showing the observed beam sizes for the science objects in arcseconds with their image size component when deconvolved from the beam with their corresponding position angles for both the beams and the resolved objects. All the objects were resolved with the exception of G310.0135+00 hence, we provide an upper limit for the source.*

From the result of our studies, there is a wide discrepancy between the spectral indices from our studies and that of Purser (2017). There could be a number of reasons for this. Firstly, the poor uv-coverage of our data (see Figure 2.2) which led to low SNR ratio for the images of the science objects. Also, Equation 3.2 Dobaczewski *et al.* (2014) used in computing the fluxes from the work of Purser

Source	Beam (AU)		Deconvolved (AU)		Luminosities (W)
	major axis	minor axis	maj. axis	minor axis	
G310	4128	1344	4128	1344	1.87×10^{12}
G332	3852	1944	10980±1080	2484±288	2.00×10^{13}
G339	2943	1458	13068±1107	1971±189	4.00×10^{12}
G345	4464	1392	4848±456	528±96	1.65×10^{13}
G345.5	12100	1560	58900±6980	9840±1020	-

Table 3.3: *Using the distance of the objects obtained from the RMS survey Lumsden et al. (2013) listed on Table 2.1, we compute the sizes of the beam and image size from Table 3.2 from arcseconds to Astronomical Units (AU) with their luminosities using the fluxes shown in Table 3.1.*

(2017) although is an appropriate procedure used by astronomers, caution must be taken when representing the spectral indices of complex regions using their integrated fluxes (i.e. when computing the flux of a source by summing up all its component parts). Although there is a wide disagreement in the spectral indices of the objects, its worthy to note that there is a close correlation from our study with that of Purser (2017) for the spectral index of G332.9868-00.4871. In addition, the positional angles of the beams are closely correlated with that of the science targets as observed in Table 3.2.

Chapter 4

Spectral Line Observation

Introduction

In this section, we present findings from our studies for both water masers and ammonia inversion transitions of the science targets. In addition, we compare our results with the H_2O Southern Galactic Plane Survey project (HOPS). The HOPS project utilized the 22 metre Mopra radio telescope to simultaneously map 100 square degrees along the southern Galactic plane, between $290^\circ \leq \ell \leq 30^\circ$ and $\mid b \mid \leq 0.5^\circ$ at 19.5 - 27.5 GHz frequencies (with central observing frequency of 24 GHz) and resolution of 135 arcseconds. The project was carried out by a consortium of international partners (see Longmore *et al.* 2017; Purcell *et al.* 2012; Walsh *et al.* 2011 for details). Mopra has a beam-width of 119 arcseconds with an average system temperature (in good weather) of $\sim$ 70 K. In order to compare the results of our studies to the HOPS data, a conversion factor of 6.41 Jy K^{-1} was used to change the main beam temperatures (units of the Mopra project) to flux density. This approach has previously been used by Urquhart *et al.* (2009), inspired by Equation (8.19) of Wilson *et al.* (2009).

4.1 Water Maser

According to Billington *et al.* (2018), water masers are found and associated with star forming regions (high and low mass environments). As a result, they are considered excellent tracers of shocked gas; often associated with molecular outflows from protostellar objects. Although the majority of the currently known water masers are associated with star forming regions, they can also be found in other galactic and intergalactic environments, including evolved stars, planetary nebulae and active galactic nuclei (AGN) (Billington *et al.* 2018; Castangia *et al.* 2017). We report the detection of water masers in all our science targets.

Using the distances listed on Table 2.1, fluxes on Table 4.2 and Equation 4.1, the computed spectral line luminosities for the science targets to determine the total power per unit bandwidth for each source radiated at 24.5 GHz are listed in Table 4.2.

$$L_\nu = 4\pi d^2 S_\nu, \tag{4.1}$$

where L_ν is the luminosity (Watts), S_ν is the flux in Jansky, (1 Jy = $10^{-26}\,Wm^{-2}Hz^{-1}$) and d is the distance in meters.

4.1.1 *G310.0135+00.3892*

The detection of a water maser in the target is reported for the first time (see Figure 4.2 for the spectra). Figure 4.3 represents the spectra from the HOPS data (extracted at coordinates 310.0134° and 0.09207°) and Figure 4.2 shows the spectra obtained using the *SPLAT* astronomical analysis tool (see Draper (2014) for details) after subtracting polynomial degree of order one as the baseline for the source. The spectra was obtained by placing a rectangular box around the water maser emission in Figure 4.4 and double clicking on the emission to obtain the spectra. The spectra obtained was done in CASA and then save as a FITS file and processed using *SPLAT*. From the spectra in Figure 4.3, the spectra appears quite noisy hence, it is likely the water maser was not detected from the HOPS project. On the other hand, from the spectra in Figure 4.2, a distinctive double emission peak is observed from our studies. The highest emission peak was detected at channel 1009 ($\sim$ velocity -35.88 km/s) and the lower emission peak was observed at channel number 1013 ($\sim$ velocity -34.18 km/s).

Although we report the detection of a water maser in the source for the first time, recently, Fedriani, R. *et al.* (2018) reported the detection of several other

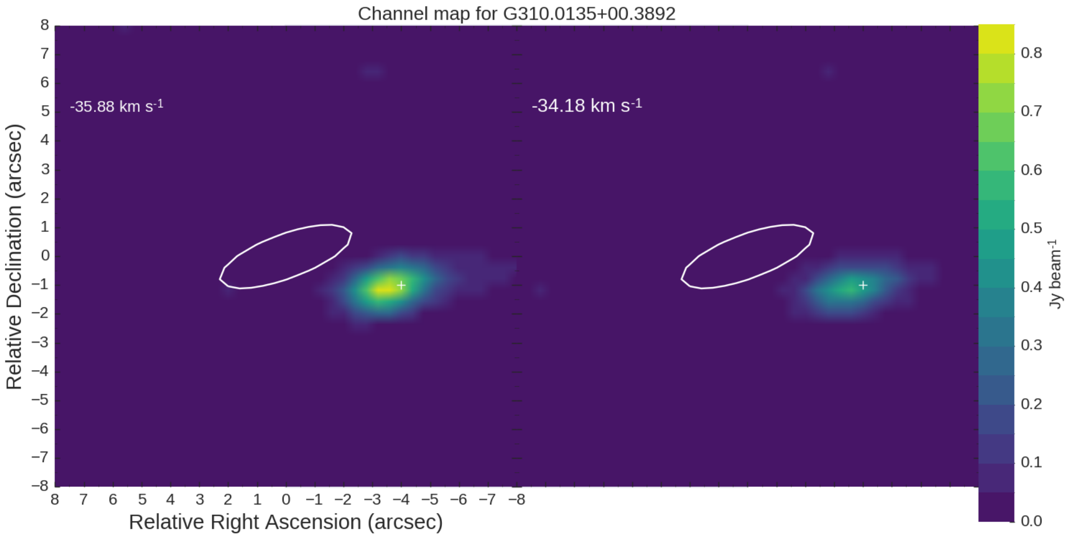

Figure 4.1: *Showing the channel maps of the position of the continuum emission (white contour, contour level is 0.01035 mJy/beam) and the water maser (indicated with the position of + sign) for G310.0135+00.3892. The colours indicate the intensities of the water maser emission.*

emission lines using NIR data from the Very Large Telescope instruments SINFONI, CRIRES and ISAAC. The authors inferred the presence of rich emission lines in the K band mainly associated with ejection and accretion processes from the spectra. In addition, H_2 emission along the parsec-scale jet was observed from the spectra. Furthermore, Brγ line was observed in the K band of the ISAAC data spectrum. According to Fedriani, R. *et al.* (2018), the Brγ emission spectra displays a P Cygni profile, and such an asymmetric line profile is indicative of an absorbing blue-shifted outflow with a measurable bulk velocity (Fedriani, R. *et al.*, 2018). The P Cygni profile for the source has a central radial velocity of 290 ± 40 km/s. The line parameters obtained from our studies through 1-D Gaussian fitting are listed in Table 4.2. The peak flux density of the highest emission at velocity of $v_{lsr} = -35.88$ km/s is estimated as $I_v = 0.14 \pm 0.01$ mJy/beam and that of the lower emission peak at central velocity, $v_{lsr} = -34.18$ km/s is esti-

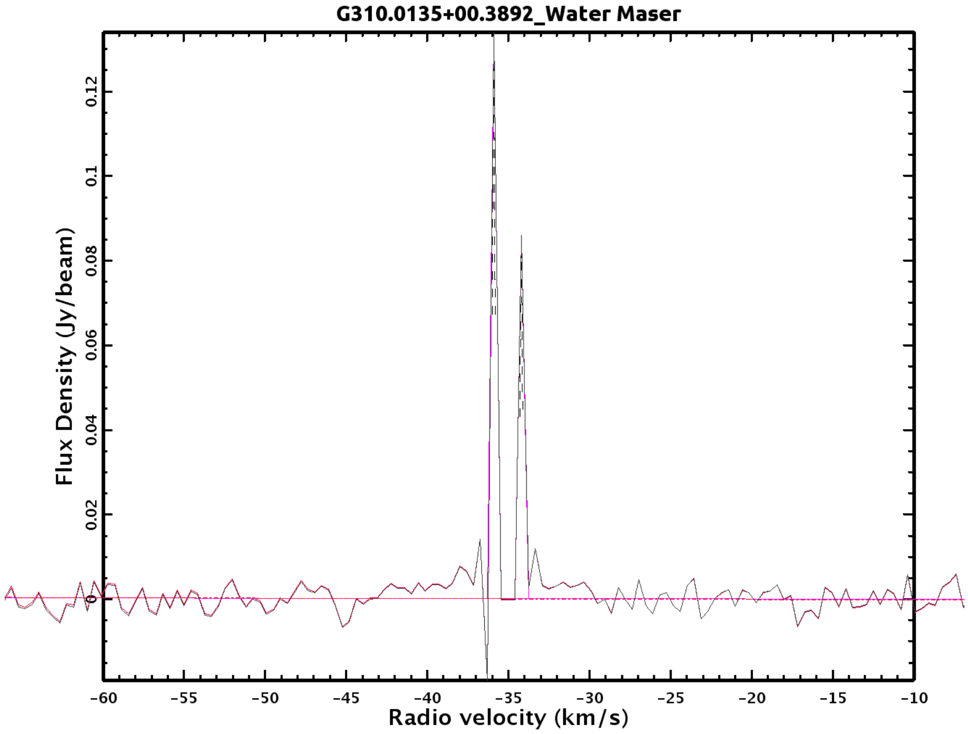

Figure 4.2: *First H_2O water maser spectra detected towards G310.0135+00.3892. The peak spectra represents the point with the strongest emission for the target.*

mated as $I_v = 0.11 \pm 0.04$ mJy/beam. Figure 4.4 the channel map represents the location of the water maser and the continuum emission. From the map in 4.4, the water maser is located at South-West of the continuum emission and is offset from the continuum emission by ~ 2 arcsec. Comparing the relative positions of the water maser and the continuum emission, the offset of the water maser from the continuum is likely caused by the presence of shocks and ejection experience during the formation process of the jet.

Several authors including Purser (2017) and Kraus *et al.* (2010) have reported that the outflows from a jet is usually within the NE-SW direction. We conclude that the water maser jet is along the NE-SW jet axis, since the disc is oriented along the NW/SE axis Kraus *et al.* (2010). The spectral line luminosity of the target has been determined to be $0.76{\times}10^{-6}L_\odot$ (see Table 4.2 for details). The computed luminosity was determined to be within the luminosity of $\sim 10^{-6}L_\odot$

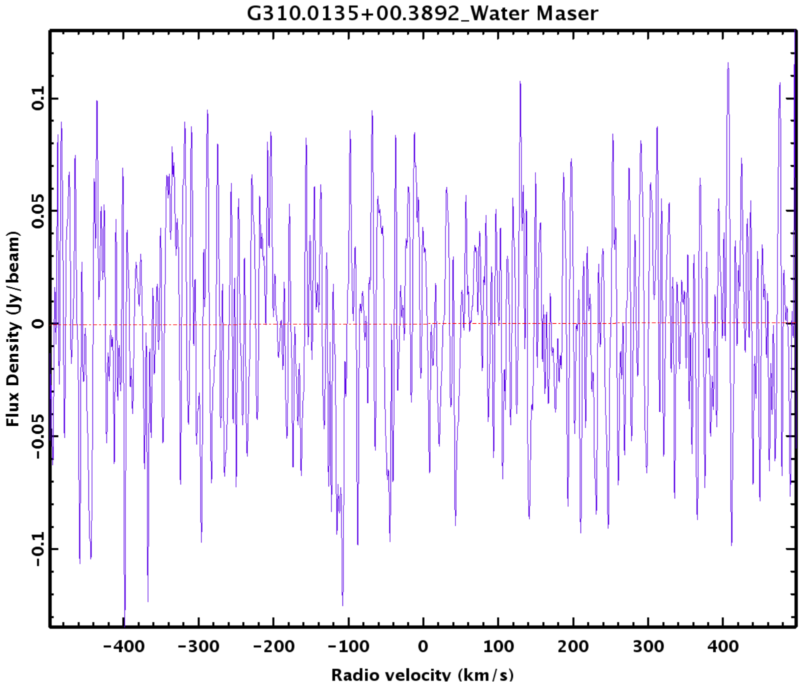

Figure 4.3: *Spectra for G310.0135+00.3892 extracted from the HOPS data (*Walsh et al., *2011). The data cube coordinates were extracted at* 310.0134° *and* 0.09207°.

of water masers found around the circumstellar regions (Lo, 2005).

The detection of a water maser in the target for the very first time indicates the presence of star forming activity in the target. In addition, the difference in local standard of rest velocities of the source from that of the detected water maser is likely caused by shocks and ejection experienced during the stars formation. According to Goddi *et al.* (2005), if the velocity is ($\leq$ 50 kms^{-1}), it is assume to be a non-dissociative (C-type) shock. Hence, we infer that the maser detected is undergoing shocks in the region. This observation is consistent with the findings of Purser (2017) for the object.

4.1.2 *G332.9868-00.4871*

The spectra for the source was extracted from the HOPS data cubes using 332.467057° and −0.260114° coordinates (see Figure 4.6 for the spectra). We report the likely detection of the G332.9868-00.4871 in both studies. The spectra in Figure 4.5 and 4.6 have similar emission peaks centred on velocities, v = -63.217 ± 0.45 and 63.22 ± 0.38 km/s respectively.

Previous work by Caswell *et al.* (2011), detected the presence of methanol masers centred on local standard of rest velocity, $v_{lsr} = -55.5$ km/s, with peak intensity of I_v=8.3 Jy/beam (see RMS survey catalogue). The methanol maser is slightly offset by 0.1 acrsec (Caswell *et al.*, 2011). In addition, Caswell *et al.* (2011) inferred that the methanol maser is being pumped by infra-red radiation.

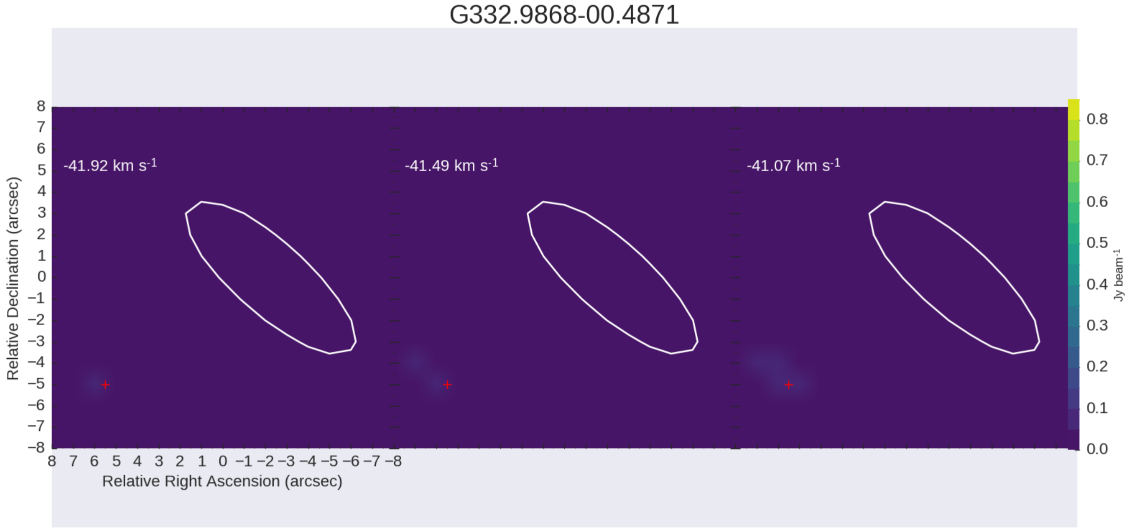

Figure 4.4: *Showing the channel maps of the position of the continuum emission (white contour, contour level is 0.004114 mJy/beam) and the water maser (position shown by + sign) for G332.9868-00.4871. The colours indicate the intensities of the water maser emission.*

The velocities of the masers observed from both studies are offset (5 km/s) from the known v_{lsr} of the source listed in Table 2.5, from the RMS survey (Lumsden *et al.*, 2013). From the channel map in 4.4, the water maser is located farther away from the continuum emission with weak peak intensity.

The line parameters obtained from our studies are listed on Table 4.2 through a 1-D Gaussian fitting with peak intensity of I_v=0.03 ± 0.003 Jy/beam, decon-

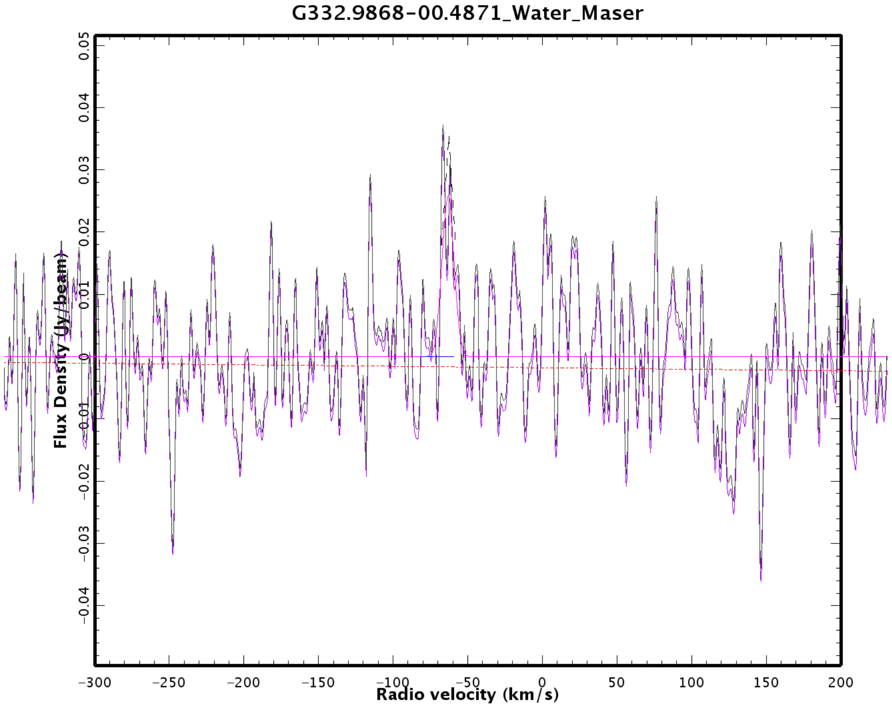

Figure 4.5: *H_2O maser spectra observed towards G332.9868-00.4871. The peak spectra represents the point with the strongest emission for the target.*

volved width 4.01 ± 0.47 km/s and $FWHM$ of $= 9.44 \pm 1.10$ km/s. On the other hand, the line parameters from the HOPS data has I_v=0.03 ± 0.002 Jy/beam, width 3.97 ± 0.38 km/s and $FWHM$ of $= 9.34 \pm 0.90$ km/s. The computed luminosity, $2.80{\times}10^{-6}L_{\odot}$, is within the expected limit of luminosity for water masers in the circumstellar regions (Lo, 2005).

4.1.3 *G339.8838-01.2588*

The water maser spectra for G339.8838-01.2588 were extracted from the HOPS data using 339.689220° and −0.065181° coordinates. The resulting spectra is shown in Figure 4.9. From the spectra, a single emission peak is observed with peak intensity, I_v=0.93±0.03 Jy/beam with central velocity, $v_{lsr} = -33.48 \pm 0.05$ km/s from the HOPS data. The peak intensity observed is lower by a factor of 2 times when compared to the peak intensity, I_v=1.85 Jy/beam reported by

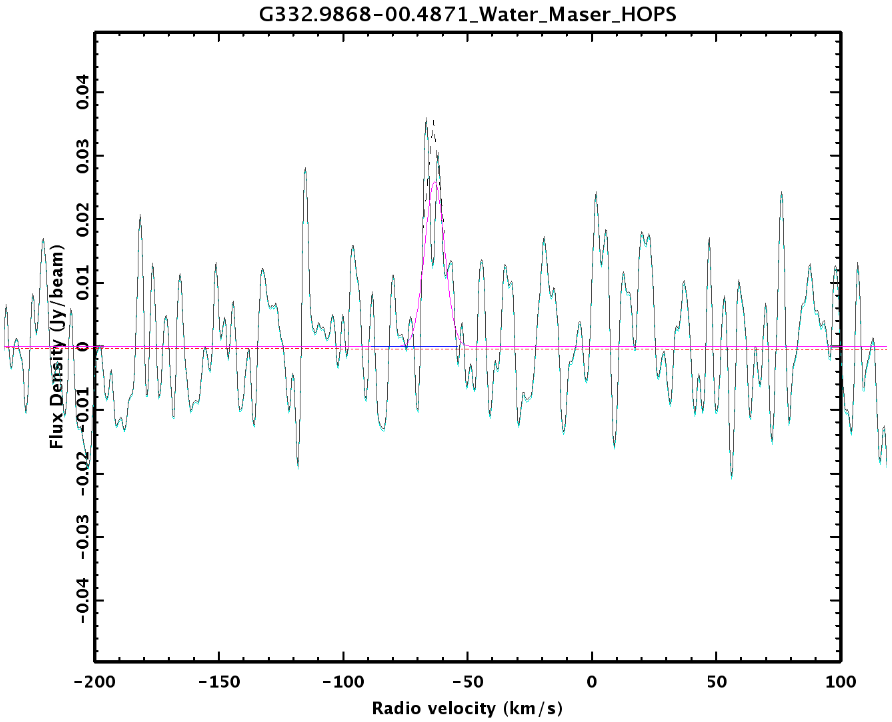

Figure 4.6: *Mopra 20 GHz observational result for G332.9868-00.4871 obtained from HOPS data (Walsh* et al.*, 2011).*

Urquhart *et al.* (2009) for the same source. In addition, a deconvolved width of 1.50 ± 0.09 km/s and $FWHM$ = 3.22 ± 0.13 km/s were obtained using a 1D Gaussian fitting.

From our work, we report the detection of five multiple maser peaks not previously observed from the HOPS result (see Figure 4.8) with the highest emission peak occurring at $v_{lsr} = -39.01 \pm 0.11$ km/s. Other parameters of the water maser for the highest emission peak are listed on Table 4.2. The point where the maser emission occurs is slightly offset when compared to the accepted v_{lsr} from the RMS survey (see Table 2.5; Lumsden *et al.* 2013). A peak intensity, I_v=3.75 ± 1.03 Jy/beam is obtained when a 1D Gaussian was fitted to the spectra. The intensity from our studies is higher by a factor of 4 times when compared with the peaks intensities from the result of HOPS and a factor of 2 times when compared with previous study of Urquhart *et al.* (2009). Additionally, the pres-

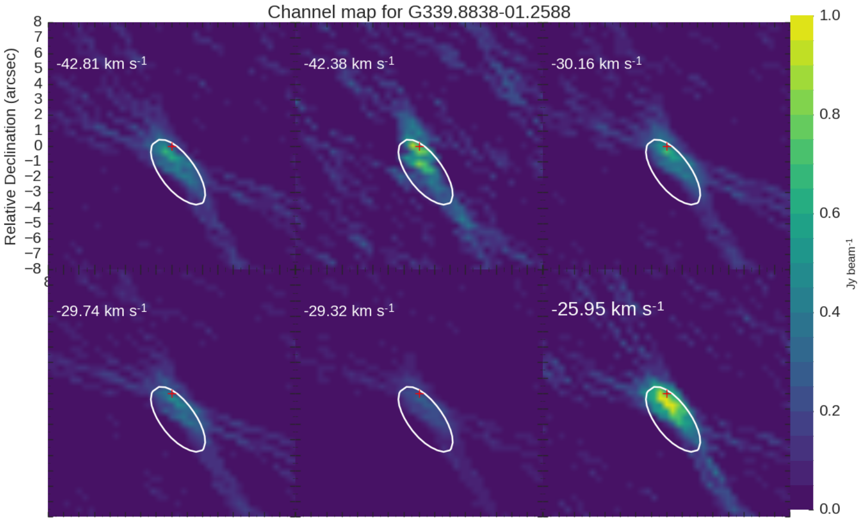

Figure 4.7: *Showing the channel maps of the position of the continuum emission (white contour, contour level is 0.0018 mJy/beam) and the water maser (indicated with the position of + sign) for G339.8838-01.2588. The colours indicate the intensities of the water maser.*

ence of several emission peaks is a possible sign of the presence of multiple masers not likely co-located. From the channel map in Figure 4.7, the water maser lies on the continuum emission in the NE and SW direction. Of the 2000 channels considered for the imaging purpose, the water maser was located at six different channels as observed from Figure 4.7. Masers are generally known to occur in few AU from the formation site due to ejection and bowshocks. This is the likely reason for the differences in the local standard of rest velocity of the water maser from the source.

The other line parameters obtained using a 1D Gaussian fitting are listed in Table 4.2. Like the previous science targets, the computed luminosity, $0.11\times10^{-6}L_\odot$ is consistent with the luminosity of $10^{-6}L_\odot$ observed for water masers located in the circumstellar regions (Lo, 2005).

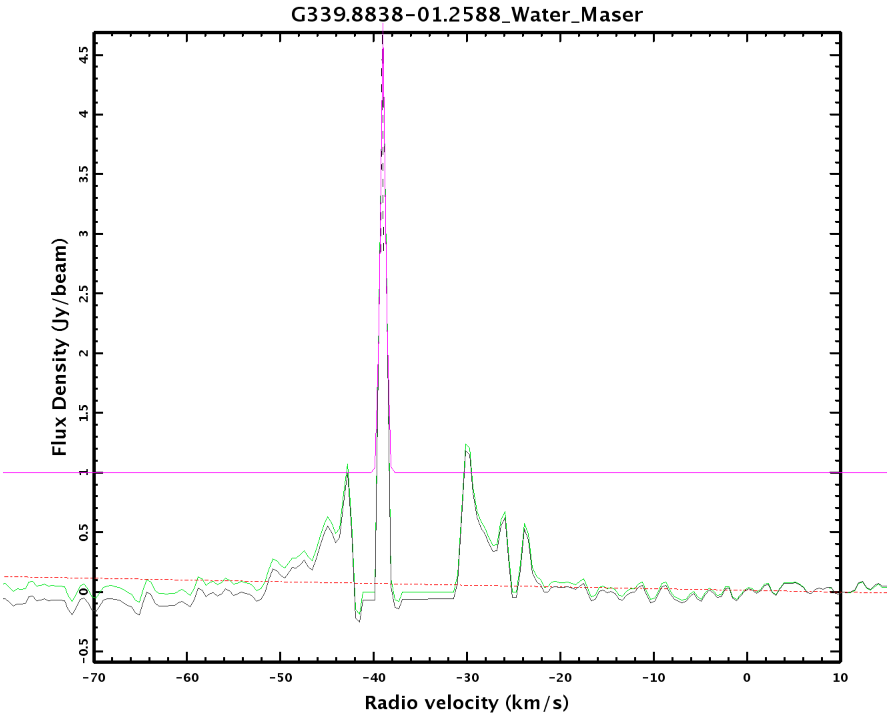

Figure 4.8: *H_2O maser spectra observed towards G339.8838-01.2588. The peak spectra represents the point with the strongest emission for the target.*

4.1.4 *G345.4938+01.4677*

Figure 4.10 shows the channel map of the continuum emission and the water maser detected for the science target. The object was observed in three channels as shown in Table 4.1. At a velocity of 5.10 km/s, the water is observed to be lying perpendicularly to the continuum emission with an offset of $\sim$ 6 arcsec. Despite the offset observed for the water maser, it has same positional orientation as the continuum lying along the North-East and South West plane as the continuum emission. It is however observed that at 6.78 km/s and 7.20 km/s, the water maser and the continuum emission lie in the same plane. The observed offset seen at 5.10 km/s is likely caused by shocks and ejections experienced by the maser during its formation.

The spectra in 4.12 was extracted using 345.316564° and 0.475764° coordinates from the HOPS data cubes. The peak intensity, I_v=0.53 ± 0.02 Jy/beam, was

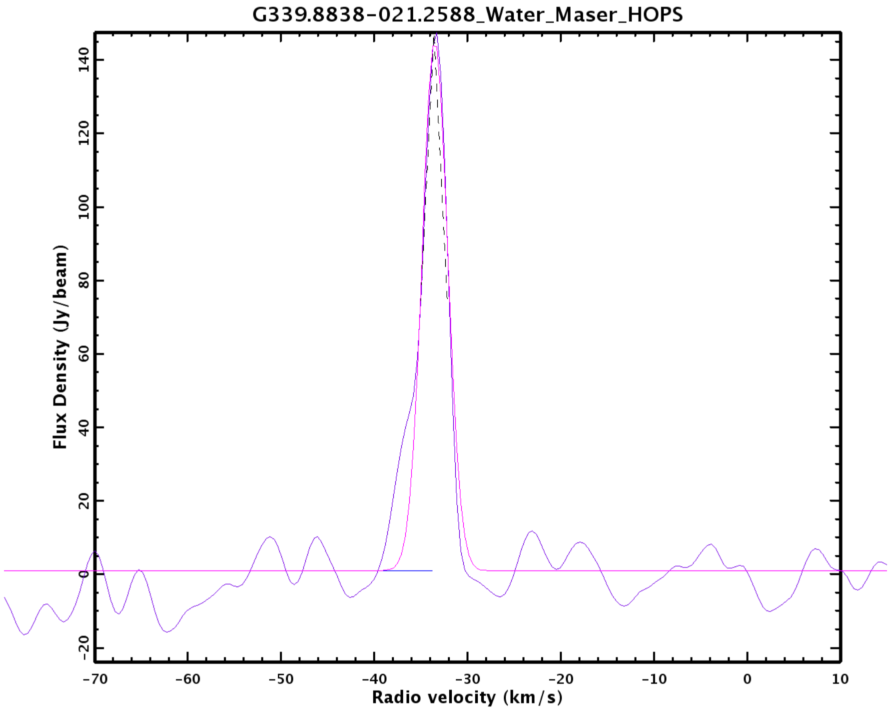

Figure 4.9: *Mopra 20 GHz observational result for G339.8838-01.2588 obtained from HOPS project* Walsh et al. *(2011).*

obtained using a 1D Gaussian fitting centred on central velocity, $v_{lsr} = -6.88 \pm 0.01$ km/s. From our studies, the double peak emission observed from the HOPS spectra is detected with the lower emission peak having emission parameters: $v_{lsr} = -16.81$ km/s and I_v=0.82 Jy/beam. Comparing the spectra in Figure 4.12 and 4.11, similar emission spectra is observed. Previous studies by Purser (2017) classified the object as jets with lobes (i.e. an eruption from the formation site with bulge lobes at the opposite ends driving out materials as they propagate through the interstellar medium). From the spectra observed in Figure 4.12, the emission is likely an absorbing blue-shifted outflow with a measurable bulk velocity as seen in previous studies by (Fedriani, R. *et al.*, 2018).

From Figure 4.11, the highest emission peak is centred on $v_{lsr} = 3.70 \pm 0.98$ km/s has a peak flux of I_v=0.125 ± 0.02 Jy/beam. The deviation (offset) of the v_{lsr} of the maser from the known v_{lsr} of the source is made evident through the

Channel number	Corresponding channel velocities (km/s)
542	5.10
546	6.78
547	7.20

Table 4.1: *A table showing the velocities of the water maser at different channels where they were observed.*

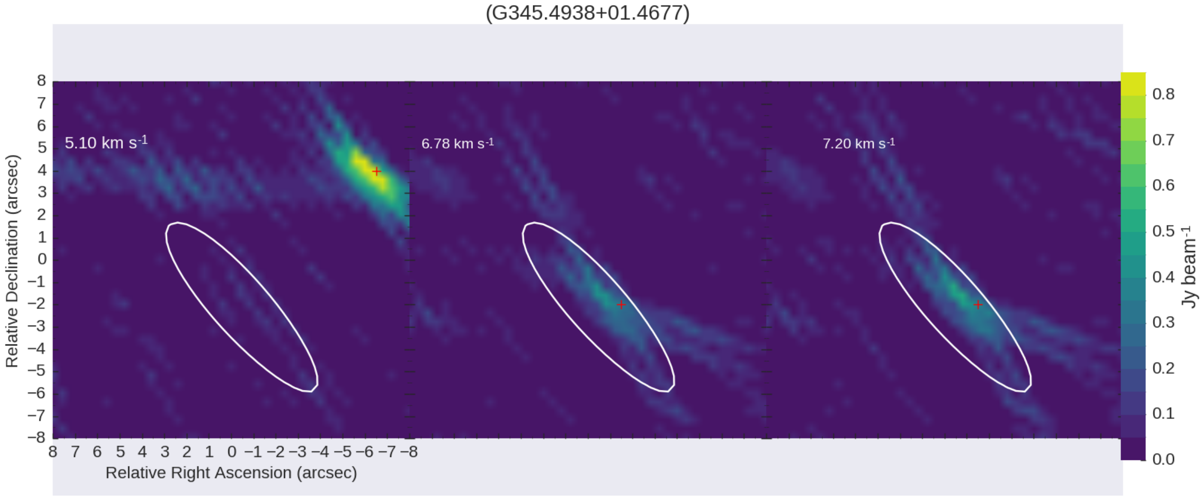

Figure 4.10: *Channel map showing the continuum emission and the* H_2O *maser for G345.4938+01.4677. The white contour represent the continuum emission with contour level at 0.0108 mJy/beam. The positions of the water masers are indicated with the red + sign.*

drift of the maser in the channel map when compared with the location of the continuum emission in Figure 4.10. The observed change of the maser velocity is in agreement with the report of Goddi *et al.* (2005) and Bally (2007). The authors infer that water masers are mostly located ∼ few hundred AU, (Goddi *et al.*, 2005) from the star forming region due to ejections and bow-shocks. Also, the computed luminosity, $0.24\times10^{-6}L_{\odot}$ is in agreement with luminosity of $10^{-6}L_{\odot}$ for water masers found within the circumstellar regions (Lo, 2005). See Table 4.2 for other line parameters of the target.

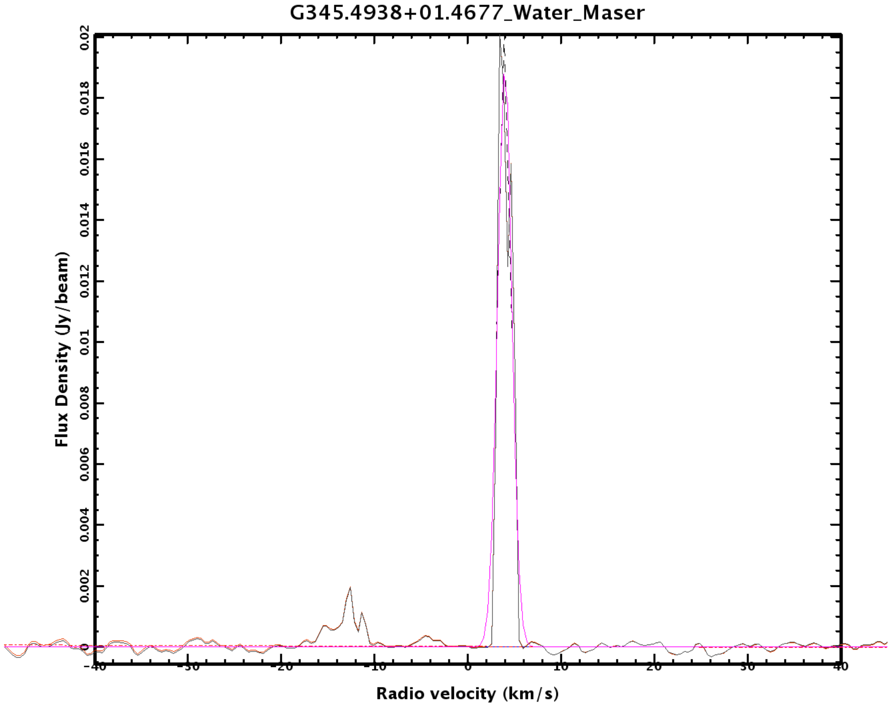

Figure 4.11: *H_2O maser spectra observed towards G345.4938+01.4677.*

Object	I_ν (mJy)	Central Velocity (km/s)	Width (km/s)	FWHM (km/s)	Flux Density (Jy/beam km/s)	Luminosity ($L_{\odot}$)
G310.0135+00	0.14±0.07	-35.88±0.07	1.38±0.58	3.26±1.37	0.11±0.06	0.76×10^{-6}
G332.9868-00	0.03±0.03	-63.17±0.45	4.01±0.46	9.44±1.10	0.26±0.04	2.80×10^{-6}
G339.8838-01	3.75±1.03	-39.01±0.11	0.29±0.87	0.67±0.19	2.68±1.06	0.11×10^{-6}
G345.4938+01	0.02±0.002	3.97±0.10	0.77±0.10	1.82±0.23	0.04±0.006	0.24×10^{-6}

Table 4.2: *Showing the line parameters obtained for the science targets after fitting 1D Gaussian to the line with the highest peak emission and the corresponding luminosities*

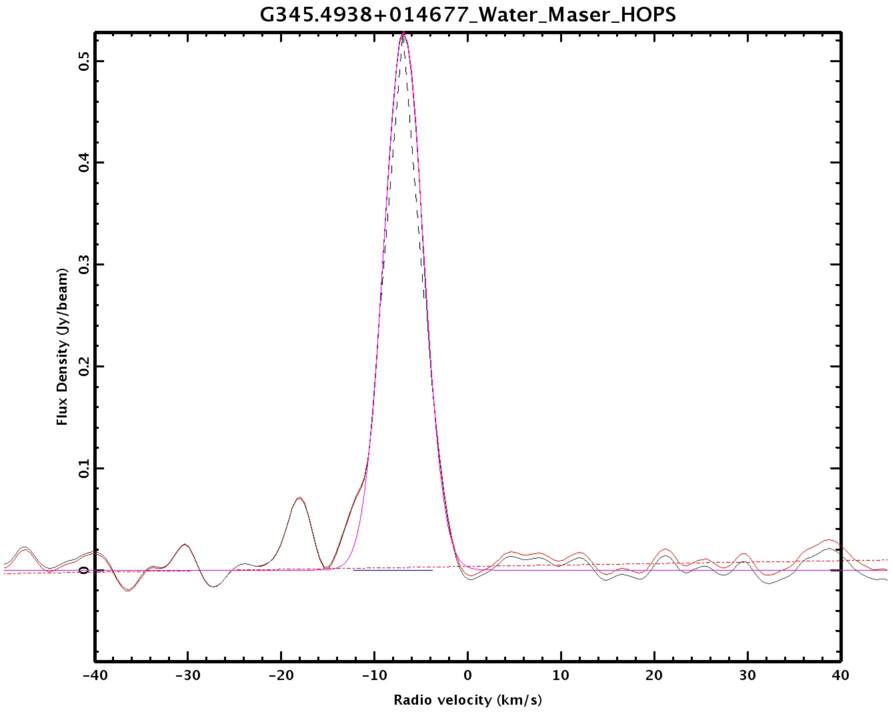

Figure 4.12: *Mopra 20 GHz observational spectral result for G345.4938+01.4677 obtained from HOPS project (Walsh et al., 2011).*

4.2 Ammonia tracers

Ammonia is a well known thermometer (i.e. molecular tracer) for estimating the temperatures of molecular gas in addition to its numerous advantages for conducting kinematic analysis. The lower ammonia transitions (i.e. NH_3 (2,2) and NH_3 (3,3)) are sensitive to cold ($\sim$ 10 - 40 K) and dense ($> 10^4$ cm^{-3}) gas and does not deplete from the gas phase at high densities ($< 10^6$ cm^{-3}). However, for all the science targets, the three para, (J,K) = (2,2), (4,4) and (5,5) and two ortho, (J,K) = (3,3) and (6,6) transitions that were observed were not detected when the coordinates were extracted from the HOPS data. Similarly, in the ATCA data, the three para, (J,K) = (2,2), (4,4) and (5,5) and two ortho, (J,K) = (3,3) and (6,6) were not detected for the science targets: G310.0135+00.3892, G332.9868-00.4871 and G339.8838-01.2588. On the contrary, the presence of (J,K) = (2,2) in the RMS survey has been observed for the aforementioned sources (see the RMS catalogue by Lumsden *et al.* 2013) with the exception of no detection reported for G345.4938+01.4677.

Although no previous detection of any ammonia transition has been observed in G345.4938+01.4677, we report the detection of ammonia para species NH_3 (2,2) as the only transition in G345.4938+01.4677 from our study (see Figure 4.13 for the intensity map over the channel map) and Figure 4.14 represents the spectra for the detection. The narrow line width of the spectra (Figure 4.14) may suggest that the emission is coming from a less extended region. A central v_{lsr} $= -15.33 \pm 0.18$ km/s was obtained using a 1D Gaussian fitting for NH_3 (2,2). The v_{lsr} obtained for the water maser is slightly offset by 2.77 km/ s relative to the v_{lsr} of the source.

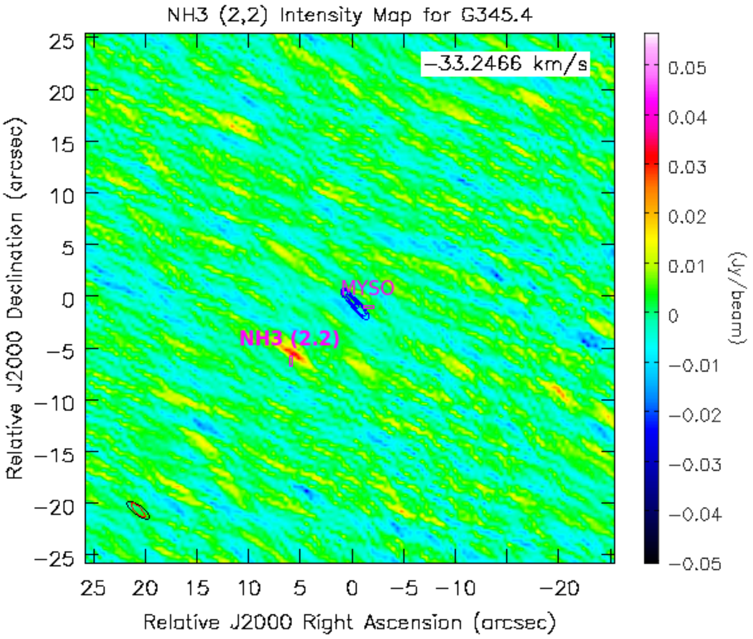

Figure 4.13: *intensity map over the channel map of NH_3 (2,2) for G345.4938+01.4677.*

The properties of the line parameters using a 1D Gaussian fitting are listed in Table 4.3.

In addition to the detection of NH_3 (2,2) in all the remaining sources from

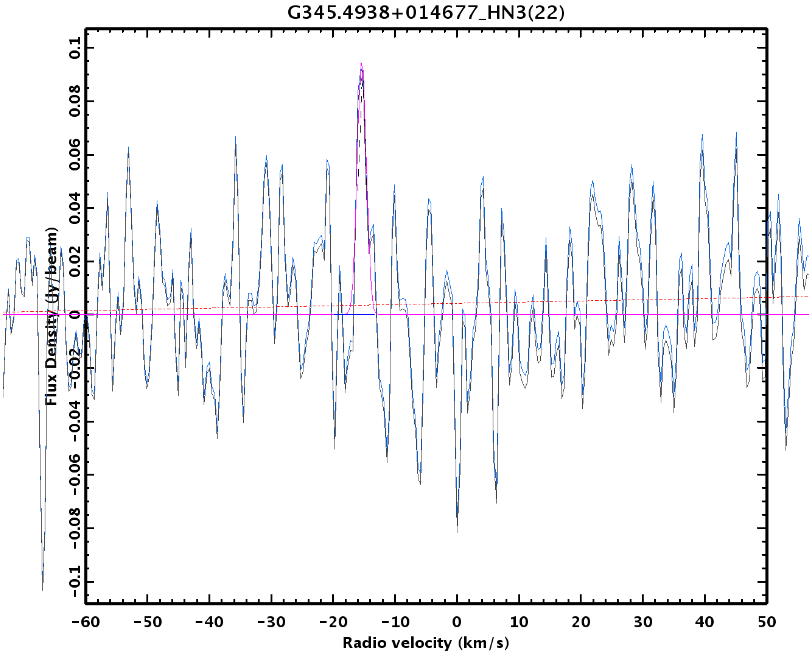

Figure 4.14: *The spectra represents the emission associated with NH_3 (2,2) for G345.4938+01.4677.*

Object	I_ν (mJy)	Central Velocity (km/s)	Width (km/s)	FWHM (km/s)	Flux (mJy/beam)
G345.4938+01	0.10±0.01	-15.37±0.12	0.71±0.12	1.68±0.28	0.17±0.04

Table 4.3: *Showing the line parameters obtained for the science targets using a 1D Gaussian fitting to the line with the highest peak emission and the corresponding luminosities*

the RMS survey by Lumsden *et al.* (2013), NH_3 (3,3) has also been reported for G339.8838-01.2588 (see Figure 4.17).

4.2.1 G332.9868-00.4871

The spectra in Figure 4.15 was obtained from data in the RMS survey with most published by Urquhart *et al.* (2015). It shows the ammonia transition for NH_3 (1,1) and NH_3 (2,2). From the Figure in 4.15 (bottom), the units on the temperature axis were changed to the standard unit of Jy/beam by using a factor of 6.41 Jy K^{-1} previously used by (Urquhart *et al.*, 2009). The properties of the obtained from the RMS catalogue has a peak intensity, I$_v$=3.78 Jy/beam and central velocity of $v_{lsr} = -31.99$ km/s and $FWHM = 3.05$ km/s. The other lines (peaks) in the NH$_3$ (1,1) transition are features associated with the inversion transition.

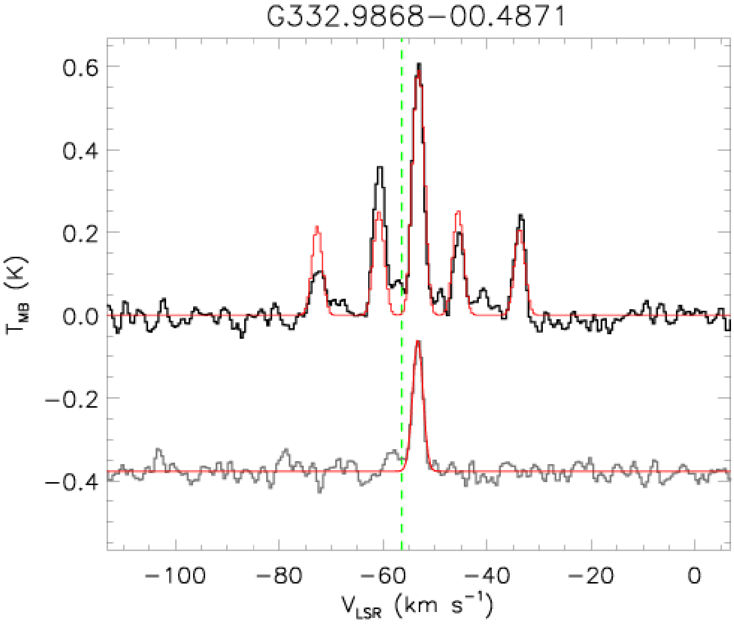

Figure 4.15: *Mopra 20 GHz observational result for NH$_3$ (1,1) and (2,2) inversion transitions top and bottom for G332.9868-00.4871. The image of the spectra was obtained from the RMS survey Lumsden et al. (2013) and as such the values on the temperature axis were converted to Jy/beam using the conversion factor of 6.41 Jy K^{-1} previously used by Urquhart et al. (2009).*

4.2.2 G339.8838-01.2588

The Figures in 4.16 and 4.17 represents the spectra for NH$_3$ (2,2) (bottom) and NH$_3$ (3,3) transitions obtained from the RMS survey by (Lumsden *et al.*, 2013). The equivalent line parameters using the conversion factors previously used by Urquhart *et al.* (2009) gives a peak intensity, I$_v$=2.05 Jy/beam and central velocity of $v_{lsr} = -53.35$ km/s. The $FWHM$ =2.31 km/s at 0.077 Jy (rms) for NH$_3$ (2,2). By estimations, a peak intensity, I$_v$=1.22 Jy/beam was obtained for NH_3 (3,3) inversion transition. The narrow line widths reported for the ammonia inversion transitions indicates a less evolved MYSO for the sources G345.4938+01.4677.

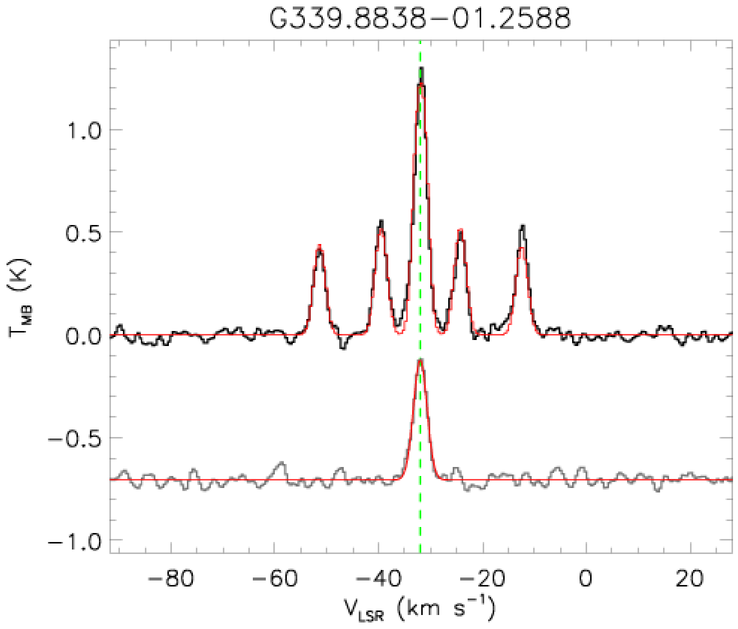

Figure 4.16: *Mopra 20 GHz observational result for NH_3 (1,1) and (2,2) inversion transitions top and bottom for G339.8838-01.2588. The image of the spectra was obtained from the RMS survey (Lumsden* et al.*, 2013).*

4.3 Summary of Ammonia Result

On the basis of the result presented for ammonia, we report non detections for the different inversion transitions for all the science objects with the exception of the NH_3 (2,2) inversion transition detected in G345.4938+01.4677 (see Figures 4.13 and 4.14 for details of the intensity channel map and spectra). Although we report non detections, ammonia inversion transition lines have been observed in the past by Lumsden *et al.* (2013) tracing cold and warm dense region of accretion disc and forming MYSOs. As a result, the ammonia lines were too extended to be detected in the 1.5 km array configuration mode.

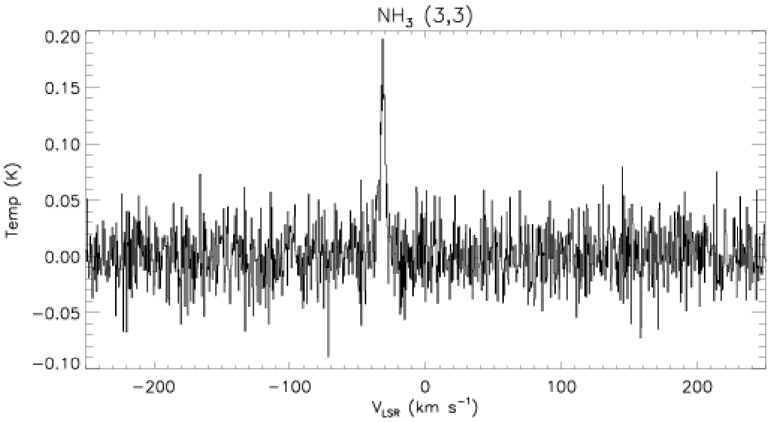

Figure 4.17: *Mopra 20 GHz observational result for NH_3 (3,3) inversion transitions for G339.8838-01.2588. The image of the spectra was obtained from the RMS survey (Lumsden* et al., *2013).*

Chapter 5

Discussion, Conclusion and Further Work.

5.1 Discussion

In this section, we present the analysis of the various results, draw conclusions and make possible recommendations for further work where applicable.

5.1.1 Research Objectives

As stated in Chapter 1, the goal of the our work was to address the following:

1 use ammonia as a diagnostic tool to resolve the disk (look for changes in the size of the disk) thereby studying the structure, composition and evolution of the star in order to look for patterns and correlations that will offer clues to how the jets vary with mass and age;

2 The properties of the radio jets (luminosities, mass loss rates, morphology) will be compared with measures of the stellar mass and age,

3 Use water masers to infer the presence of star forming activities and how the offset of the water maser relates to the jet of the object.

5.1.2 Radio Continuum Emission.

The sources were previously studied at radio continuum by Purser (2017). Using the ATCA telescope in the 6 km baseline configuration mode at 5, 9, 17 and 24.5 GHz observing frequencies. The similarity of our work to the work of Purser (2017) is the use of 24.5 GHz frequency band for both studies. The observation of our science targets was however performed in the 1.5 km configuration mode. In this array configuration, we expected to observe faint extended structures normally resolved out at higher resolutions.

From the results of our studies, the flux densities obtained using a Gaussian fit is in close agreement with flux densities reported by Purser (2017) (see Table 3.1 for details). Furthermore, most structures of the sources observed at lower observing frequencies (i.e. 5, 9, 17 GHz) were mostly not detected due to low sensitivity level ($\sigma \sim 0.10 - 0.58$ mJy/beam) in our data when compared to the work of Purser *et al.* (2016) whose sensitivity level was $73 - 106$ μJy/beam. For details of the fluxes, sizes (major and minor axes), position angles, luminosity and spectral index, see Table 3.1, 3.2 and 3.3 for details. The SEDs of all the four science targets showed a positive spectral index with G339.8838-01.2588 having a spectral index of $\alpha = -0.01 \pm 0.11$ reported for the source. This value is consistent with an H II region. Consequently, we infer the presence of an H II region in the source. This observation is in agreement with the findings of Purser (2017).

In addressing the goal 2 of work, luminosities were computed (see Table 3.2) for all science targets and were found to be very bright at radio wavelengths with G332.9868-00.4871 proving to be most luminous with a luminosity value of 2.00×10^{13} W. On the other hand, the luminosity of G310.0135+00.3892 was determined as 1.87×10^{12} W with mass loss rate of ($\sim 1.8 \times 10^{-5} M_{\odot}$ yr^{-1}, Purser *et al.* 2016) and age of $\sim 6 \times 10^{4}$ years (Fedriani, R. *et al.*, 2018). Morphologically, G310.0135+00.3892 and G345.4938+01.4677 were found to be bright central compact objects. In addition, G332.9868-00.4871 and G339.8838-01.2588 were observed to possess elongated structures with positional orientation in the NE-SE and NW-SW directions. The elongated structures observed in G332.9868-00.4871 and G339.8838-01.2588 indicates the likely presence of jets transporting materials from the formation site to the interstellar medium.

5.1.3 Spectral Line Emission

Water Masers.

For our stated research goal 3, spectral line observation of four MYSOs have been successfully carried out. We detected the presence of water masers in all the sources. The luminosities of the water masers computed were found in the range of $0.11 - 2.80 \times 10^{-6} L_{\odot}$. According to Lo (2005), the spectral luminosity of water masers located in the circumstellar region of the MYSOs are in the order of $10^{-6} L_{\odot}$ and those located at the core are estimated as $10^{-4} L_{\odot}$. Consequently, the computed luminosities of the water masers in the sources lie within the circumstellar range. Hence we conclude that the water masers are within the circumstellar region (Lo, 2005).

Furthermore, the detection of water masers in all science targets confirms the presence of star forming activities especially in G310.0135+00.3892 where it was detected and reported for the first time. It was observed that all water masers were positionally offset when compared to their respective continuum emissions. This offset of the water maser from their continuum emission leads to positional displacement from their known local standard of rest thereby assuming the velocity of their new position. This resulted in the observed differences in the local standard of rest velocities of the water masers when compared to the v_{lsr} of their sources. This observation is consistent with the findings of Goddi *et al.* (2005) and Bally (2007), where it was inferred that water masers emission likely originates close (with a few hundred AU) to a forming MYSOs.

A unique case in our results is the detection of a water maser in the target G310.0135+00.3892. This detection is of particular interest because it is the first ever detection reported for the object. The outflow is likely emanating from the envelopes of the jets. Authors including Purser (2017) reported that the outflow from the jet is within the NE-SW direction. Taking inspiration from Purser (2017), we conclude that the water maser jet is along the NE-SW jet axis, since the disc is oriented along the NW/SE axis (Kraus *et al.*, 2010). The offset of the water maser informs us of the orientation of the disc along the jet axis of the object.

Furthermore, from the results of the spectral profile reported for the water masers, multiple emission peaks are observed. The presence of the multiple peaks indicates the presence of multiple maser features not spatially co-located and this is informs us of high degree of collisions (high density and pressure) leading to the pumping and creation of more water maser spots around the core of the MYSO formation site. The water maser located in G339.8838-01.2588 has previously been detected by Urquhart *et al.* (2009) with marginal differences in their flux density.

Ammonia.

Finally, the last aim of our study was to "use ammonia as a diagnostic tool to resolve the disk (look for changes in the size of the disk) thereby studying the structure, composition and evolution of the star in order to look for patterns and correlations that will offer clues to how the jets vary with mass and age". Numerous studies have pointed out the importance of ammonia as a molecular tracer. According to Urquhart *et al.* (2015), ammonia inversion transition (NH_3 (J,K) = (2,2)) is sensitive to cold ($\sim$ 10 - 40 K) and less dense ($< 10^4$ cm^{-3}) regions. From our studies, other inversion transition lines (NH_3 (J,K) = (2,2), (3,3), (4,4), (5,5) and ((6,6)) were not observed in the scource likely due to the sources being too extended (faint). For the source G345.4938+01.4677, we however report the detection of NH_3 (2,2) inversion transition. However, para species NH_3 (2,2) has previously been detected in G310.0135+00.3892, G332.9868-00.4871 and G339.8838-01.2588. In addition, the ortho inversion transition NH_3 (3,3) has been detected in G339.8838-01.2588. Based on the narrow line width of the spectra, we infer the presence of emission coming from a less extended region (Ao *et al.*, 2011) since larger line widths are associated with more evolved protostars generally attributed to increased feedback from embedded objects (Urquhart *et al.*, 2015). Although Mopra data from the RMS survey had previously detected the NH_3 (2,2) transition for the sources, we were not able to detected these sources probably because the sources were spread out across the beam rather than a more compact source that is expected.

From the ammonia results, the use of ammonia as a diagnostic tool to resolve the disk (look for changes in the size of the disk) thereby studying the structure, composition and evolution of the star in order to look for patterns and correlations that will offer clues to how the jets vary with mass and age was not achieved because the inversion transition were not detected for the various science objects with the exception of G345.4938+01.4677 in which the NH_3 (J,K) = (2,2) ammonia inversion transition was reported.

5.2 Conclusion

Radio studies (continuum and spectral line emission) have been carried out for five MYSOs using data obtained from the ATCA. Of the five MYSOs selected, only four were detected with flux density in the range of $\sim 0.10 - 0.58$ mJy/beam. The flux density values obtained from our studies were observed to be in close agreement with previous study by Purser (2017). From his work, flux density values in the range of $73 - 106$ μJy/beam were reported. A further plot of the SEDs revealed the presence of thermal and H II regions in the sources. Three out of the four science targets showed thermal emission and one showed non thermal emission with the possible presence of an H II region having a spectral index, $\alpha = -0.01 \pm 0.11$. With a synthesised beam of ~ 2 arcsec, it was expected that more features (other objects in the region) would be observed from our studies. However, less structures were observed as a result low sensitivity level compared to the sensitivity level of Purser (2017).

Further studies of the objects using spectral line emission revealed the presence of a water maser in all our detected science targets. The detection of a water maser in the object G310.0135+00.3892 is detected for the very first time. The water maser detected in G310.0135+00.3892 was found to be lying along the NE-SW of the jet axis, since the disc is situated along the NW-SE axis of the outflow. The v_{lsr} of the water maser in all our science targets were observed to be offset on the average by ~ 2 km/s from the expected v_{lsr} of the source. This observation is however consistent with the reported behaviours of water masers (they are found a few hundred AU from the formation site of a forming MYSO) as reported by Goddi *et al.* (2005) and Bally (2007). The computed spectral luminosities of

$0.11 - 2.80 \times 10^{-6} L_{\odot}$ were obtained for the water maser reveals that the masers are within the circumstellar region estimated in the order of $10^{-6} L_{\odot}$ (Lo, 2005). In addition, the presence of multiple water maser emission were observed for the sources, indicating the presence of multiple emission peaks from collision of the masers and the jets due to high density and pressure around the core and are not spatially co-located (i.e. found in different areas of the forming MYSO).

In addition to the detected water maser, we detected NH_3 (2,2) in the source G345.4938+01.4677. Contrary to earlier detection of NH_3 (2,2) transition for the remaining sources by Lumsden *et al.* (2013) in the RMS catalogue, it was not detected from our studies. The spread of the source over the beam could be the likely reason for the non detections. Hence, we infer that the ammonia inversion transition is tracing the outer gas in the envelope.

Based on our objectives outline in the previous chapters and sections, we have been able to achieve two namely

- The properties of the radio jets (luminosities, mass loss rates, morphology)
- Use water masers to infer the presence of star forming activities and how the offset of the water maser relates to the jet of the object

As a result, we conclude that we have successfully determined the sizes, luminosities, morphology and have found how the water masers relates to the jet. This has improved our understanding of how masers are pumped and moved away from the formation site, the accretion process, the timeline of the formation process and the direction of the disk and jets in massive star formation processes. We therefore conclude that 2/3 objectives were achieved although we report the non detection of ammonia inversion transitions from our studies.

5.3 Further Work

We have successfully carried out radio studies of four out of the five massive young stellar objects selected from the RMS survey based on their bolometric luminosities, $L_{bol} > 20000L_{\odot}$, declination, $\delta < 40°$ and distances d$\leq 3kpc$. In addition, the sources selected with these criteria are far too south to be observed with the VLA and the sources can also be observed with ALMA in future for complementary studies. Furthermore, all sources chosen for our consideration have been well studied by Purser (2017) at radio continuum. The RMS survey contains over 2,000 MSX and 2MASS colour selected MYSO candidates. By way of enhancing and extending the work on the spectral line observation in Chapter 4, proposal for more telescope time can be made for more work to be done on the remaining MYSOs that Purser (2017) studied for his PhD. The work can also be extended to the northern hemisphere through the use of VLA telescopes to carry out spectral line studies of MYSOs.

In addition, with the advent of the MeerKAT telescope in South Africa fully operational, proposal for telescope time can be made for the study of more MYSOs in the southern hemisphere. MeerKAT also has a better *uv*-coverage due it numerous telescopes when compared to the ATCA telescope. The relationship between the spectral line luminosities and bolometric luminosities of the sources were not established due to the limited number of sources considered for our studies.

Appendix A

Data Reduction Code and Python Script.

A.1 CASA Data Reduction Code

```
CASA CODES FOR ATCA DATA REDUCTION.
listobs(vis=’2014-10-combined’, verbose=T,listfile=’file_with_listobs_output’)

flagdata(vis=’2014-10-combined’, flagbackup=T, mode=’tfcrop’)

flagdata(vis=’ 2014-10-combined’, flagbackup=T,  mode=’rflag’)

###creates a manual model for scaling fluxes###.
setjy(vis=’2014-10-combined’, standard =’manual’, field=’1’, spw =’’,
reffreq=’24.5GHz’,fluxdensity=[0.7291,0,0,0] , spix=[-1.3763])

##Initial Phase Calibration##

#For the calibrators#
gaincal(vis=’2014-10-combined’,caltable=’2014-10.G0all’,field=’0,1,3,5’,
refant=’CA04’, spw=’’,gaintype=’G’,calmode=’p’, solint=’6s’, minsnr=5)

plotcal(caltable=’2014-10.G0all’,xaxis=’time’,yaxis=’phase’,
poln=’R’,iteration=’antenna’,plotrange=[-1,-1,-180, 180])
```

```
gaincal(vis='2014-10-combined',caltable='2014-10.G0', field='0,3',

refant='CA04', spw='',calmode='p', solint='6s', minsnr=5)

plotcal(caltable='2014-10.G0',xaxis='time',yaxis='phase',poln='R',
field='0',iteration='antenna',plotrange=[-1,-1,100,100])

##Delay Calibration##

gaincal(vis='2014-10-combined',caltable ='2014-10.K0',field='0,3',
refant='CA04',spw='',gaintype='K',solint='6s',
combine='scan',minsnr=5,gaintable=['2014-10.G0'])

##Bandpass Calibration##
bandpass(vis='2014-10-combined',caltable='2014-10.B0',field='0,3',spw='',
refant='CA04',solnorm=True,

combine='scan', solint='6s',bandtype='B',gaintable=['2014-10.G0', '2014-10.K0'])

##BANDPASS PLOT##
plotcal(caltable= '2014-10.B0',poln='R', xaxis='chan',yaxis='amp',
field= '0,3',subplot=331,iteration='antenna'
,figfile='plotcal_4c2935-B0-R-amp.png')

plotcal(caltable= '2014-10.B0',poln='R', xaxis='chan',yaxis='phase',
field= '0,3',subplot=331,iteration='antenna',
figfile='plotcal_4c2935-B0-R-phase.png')

##Gain Calibration##
##For phase##
gaincal(vis='2014-10-combined',caltable='2014-10.G1',field='5~6',spw='',
solint='6s',refant='CA04',gaintype='G',calmode='ap',
gaintable=['2014-10.K0','2014-10.B0/'],interp=['linear','linear','nearest'])

##For flux##
```

```
gaincal(vis='2014-10-combined',caltable='2014-10.G1',field='4',spw='',
solint='6s',refant='CA04',gaintype='G',calmode='ap',
gaintable=['2014-10.K0','2014-10.B0'], append=True)

##For Bandpass##
gaincal(vis='2014-10-combined',caltable='2014-10.G1',field='1,5',spw='',
solint='6s',refant='CA04',gaintype='G',calmode='ap',
gaintable=['2014-10.K0','2014-10.B0/'], append=True)

##Scaling the Amplitude Gains##
myscale = fluxscale(vis='2014-10-combined',
caltable='2014-10.G1', fluxtable='2014-10.fluxscale1',
reference=['4'],   transfer=['0,1,3,5'], incremental=False)

plotcal(caltable='2014-10-09_0624.C2935.merge.fluxscale1',
xaxis='time',yaxis='amp',poln='R',figfile='plotcal_4c2935-fluxscale1-amp-R.png')

##Applying the Calibration##
applycal(vis='2014-10-combined',field='2,4',
gaintable=['2014-10.fluxscale1', '2014-10.K0','2014-10.B0/'],
gainfield=['2','',''], interp=['linear','',''],
calwt=[False],  parang=True)

applycal(vis='2014-10-combined',field='3'',gaintable=['2014-10.fluxscale1',
'2014-10.K0','2014-10.B0/'],
gaincal(vis='2014-10-combined',caltable='2014-10.G1',field='4',spw=''
,solint='6s',refant='CA04',gaintype='G',calmode='ap',
gaintable=['2014-10.K0','2014-10.B0'], append=True),

gainfield=['2','',''], interp=['linear','',''], calwt=[False],
parang=True)

plotms(vis='2014-10-combined',field='0',correlation='XX,YY',timerange='',
antenna='',avgtime='60', xaxis='phase',xdatacolumn='corrected',yaxis='amp',
ydatacolumn='corrected',plotrange=[-180,180,0,3],coloraxis='corr',
plotfile='plotms_4c2935-fld0-corrected-ampvsphase.png')
```

```
##SPLIT##:
split(vis=’2014-10-combined’,outputvis=’sources’,
datacolumn=’corrected’,field=’3,5˜8’)


##Initial Imaging##
plotms(vis=’4c2935.ms/’,xaxis=’uvwave’,yaxis=’amp’,
ydatacolumn=’data’, field=’0’,avgtime=’30’,correlation=’XX’,
plotfile=’plotms_3c391-mosaic0-uvwave.png’,overwrite=True)


split(vis=’2014-10-09.C2935.ms.merge’,outputvis=’G310-0135.ms’,
datacolumn=’corrected’,field=’3,5˜7’)

clean(vis=’G310-0135.ms’,imagename=’G310-0135_noms_I’,field=’3’,
spw=’’,mode=’mfs’,niter=50000, gain=0.1, threshold=’0.01mJy’,
psfmode=’clark’, imagermode=’csclass’, ftmachine=’mosaic’,
multiscale=[0],  interactive=True, imsize=[512,512],
cell=[’0.10arcsec’,’0.1arcsec’],
stokes=’I’,weighting=’briggs’,robust=0.5, usescratch=False)
```

A.2 Python Code for SED Plots

```
import matplotlib.pylab as plt
import numpy as np
from scipy.optimize import curve_fit
def power_law(x,m,c):
    return x * m + c

#Raw-coded data
freqs = np.array([5.5,9.0,17.0,22.8,24.5])
fluxes = np.array([1.2, 1.35, 1.65, 1.89,1.53])
flux_errs = np.array([0.3, 0.13, 0.1, 0.16,0.08])
```

```
#freqs = np.array([1.517, 5.799, 44.0])
#fluxes = np.array([3.55e-4, 2.7e-4, 6.84e-4])
#flux_errs = np.array([8.9e-5, 1.9e-5, 6.2e-5])

#Add in absolute flux-scale 10% uncertainties for ATCA K band.
flux_errs += fluxes * [0.1, 0.1, 0.1, 0.1,0.1]

#Calculate logarithmic errors
flux_log_errs = flux_errs / (np.log(10.) * fluxes)

plt.close('all')

fig = plt.figure(figsize=(3.15,3.15))

plt.plot(np.log10(freqs[:4]), np.log10(fluxes[:4]), 'bs')
plt.plot(np.log10(freqs[4]), np.log10(fluxes[4]), 'go')
plt.errorbar(np.log10(freqs), np.log10(fluxes),
yerr=flux_log_errs, fmt='None', ecolor='b')
#plt.axis('equal')
plt.legend(loc=0)

#Fit for spectral index
c1 = np.log10(fluxes[2]) - np.log10(freqs[2]) * 0.6
flux_diffs = fluxes - 10**power_law(freqs, 0.6, c1)

coeffs,covmat = curve_fit(power_law, np.log10(freqs), np.log10(fluxes),
p0=None,sigma=flux_log_errs, absolute_sigma=True)
variances     = covmat.diagonal()
std_devs      = np.sqrt(variances)

#Print fit results
print("\nYour line fit equation is of the form y=A * x**b, y = " +
      format(coeffs[1],'.2f') + ' * x**'+format(coeffs[0], '.2f') + '')
print("\nThe value of A is
"+format(coeffs[1],'.2f')+"+/-"+format(std_devs[1],'.2f'))
print("\nYour spectral index is:
```

```
"+format(coeffs[0],'.2f')+"+/-"+format(std_devs[0],'.2f'))

#Plot fitted power-law for spectral index
xs = np.linspace(*plt.xlim())
plt.plot(xs, power_law(xs,*coeffs), 'r-')

plt.title('SED for G310.0135+00.3892', size=24)
plt.xlabel('Frequency (Hz)', size=22)
plt.ylabel('Flux (mJy)', size=22)
#plt.xscale('log')
#plt.yscale('log')
plt.show()
```

A.3 Python Code for Channel Maps plotting

```
##########################################################################
#                    channel maps plotting script                        #
##########################################################################
#%pylab inline
import matplotlib
from matplotlib.pylab import *
import pyfits as pf
from matplotlib.ticker import *
import numpy as np
import matplotlib.font_manager
from matplotlib.patches import Ellipse as ellipse
import seaborn as sns;
from matplotlib.colors import ListedColormap;
%pylab


# Set conversion factors
cm2km = 1e-5

# Set constants and parameters (in cgs/astronomy units)
ckm  = 2.99792458e5   # cm/km
```

```
# keplerian mask
fits_chan = '/home/kojo/Desktop/chapter4plots/G310-H20.fits'


# read the header from the observed FITS image
head = pf.getheader(fits_chan)

# generate x and y axes: offset position in arcsec
nx    = head['NAXIS1']    # width of image in pixels
xpix  = head['CRPIX1']    # reference pixel coordinates
xdelt = head['CDELT1']    # width of a pixel in data units

ny    = head['NAXIS2']    # height of image in pixels
ypix  = head['CRPIX2']    # reference pixel coordinates
ydelt = head['CDELT2']    # height of a pixel in data units

# convert from degrees to arcsecs
xval = ((arange(nx) - xpix + 1) * xdelt)*3600
yval = ((arange(ny) - ypix + 1) * ydelt)*3600

# create channel axis (Hz)
nv    = head['NAXIS3']
vpix  = head['CRPIX3']
vdelt = head['CDELT3']
vval  = head['CRVAL3']
vel = (((arange(nv) - vpix + 1) * vdelt) + vval)/1000.

# extract rest frequency (Hz)
freq  = head['RESTFRQ']

# source velocity (km/s)


# convert from frequency (Hz) to LRSK velocity (km/s) using
# rest frequency and source velocity
```

```
#for i in range(nv):
    #vel[i] = (ckm*((freq-vel[i])/freq))

# create dictionaries containing axes and images
img_chan = {'image':squeeze(pf.getdata(fits_chan)),
'ra_offset':xval, 'dec_offset':yval}
#img_mask = {'image':squeeze(pf.getdata(fits_mask)),
'ra_offset':xval, 'dec_offset':yval}

# for plotting colour map of data
masked_img_chan = np.ma.array(img_chan['image'],
mask=np.isnan(img_chan['image']))
#masked_img_mask = np.ma.array(img_mask['image'],
mask=np.isnan(img_mask['image']))

# set spacing between axes labels and tick direction
rcParams['ytick.major.pad'] = 6
rcParams['xtick.major.pad'] = 6

rcParams['xtick.direction'] = 'in'
rcParams['ytick.direction'] = 'in'

rcParams['xtick.major.size'] = 5
rcParams['xtick.minor.size'] = 2.5
rcParams['ytick.major.size'] = 5
rcParams['ytick.minor.size'] = 2.5

rcParams['ytick.labelsize'] = 16
rcParams['xtick.labelsize'] = 16

# font type
matplotlib.rc('font', family='sans-serif')
matplotlib.rc('font', serif='Helvetica Neue')
matplotlib.rc('text', usetex='false')
matplotlib.rcParams.update({'font.size': 16})
```

```
#set seaborn plot styles
#sns.set_style("white")
#sns.set_style("ticks")

#set figure size and create image canvas (in cm)
fig = figure(figsize=[12,6])
ax  = fig.add_subplot(111)

plt.title('Channel map for G310.0135+00.3892',fontsize=19)

ax.axis('scaled')
# remove tick labels from main grid
ax.set_xticklabels([])
ax.set_yticklabels([])
ax.set_xticks([])
ax.set_yticks([])

# adjust spacing between subplots
plt.subplots_adjust(wspace=0,hspace=0)

# Set axes limits (arcsec)
xmin = -8
xmax =  8
ymin = -8
ymax =  8

fits_cont = '/home/kojo/Desktop/chapter4plots/G310-cont.fits'

img_cont = {'image':squeeze(pf.getdata(fits_cont)),
'ra_offset':xval, 'dec_offset':yval},
masked_cont = np.ma.array (img_cont['image'], mask=np.isnan(img_cont['image']))

# Mask ra and dec for calculating contours
ra = np.array(img_chan['ra_offset'])
ra[ra>xmax] = np.nan
```

```
ra[ra<xmin] = np.nan

dec = np.array(img_chan['dec_offset'])
dec[dec>ymax] = np.nan
dec[dec<ymin] = np.nan

# Set contour level
rms = 0.0115
contlev = np.array([0.9])
contlev = contlev*rms



# Set physical range of colour map
cxmin = img_chan['ra_offset'][0]
cxmax = img_chan['ra_offset'][-1]
cymin = img_chan['dec_offset'][-1]
cymax = img_chan['dec_offset'][0]

cbmin=-0.0
cbmax=0.85001
cbtmin=0.05
cbtmaj=0.1
cbnum=int((cbmax-cbmin)/cbtmin)

colormap =  ListedColormap(sns.color_palette("viridis",cbnum))
source=0.0
# Loop over channels and plot each panel
for i in range(2000):

    chan1 = 1009 #1009
    chan2 = 1013 #1037

    if i==chan1:
        ax  = fig.add_subplot(1,2,1)
        velocity = '%4.2f' % (vel[chan1]-source)
        ax.grid(False)
```

```
        ax.axis([xmax,xmin,ymin,ymax],’scaled’)
        majorLocator = MultipleLocator(1.0)
        ax.xaxis.set_major_locator(majorLocator)
        ax.yaxis.set_major_locator(majorLocator)
        minorLocator= MultipleLocator(.5)
        ax.xaxis.set_minor_locator(minorLocator)
        ax.yaxis.set_minor_locator(minorLocator)
        ax.set_xlabel(’Relative Right Ascension (arcsec)’,x=.5, fontsize=21)
        ax.set_ylabel(’Relative Declination (arcsec)’,y =.5, fontsize=21)
        #beam_ellipse_color = ’white’
        #bmin = head[’bmin’]*3600.
        #bmaj = head[’bmaj’]*3600.
        #bpa  = head[’bpa’]
        #el   = ellipse(xy=[2,-2], width=bmin, height=bmaj, angle=-bpa,fc=’blue’,
        ec=’blue’, fill=True, zorder=10)
        #ax.add_artist(el)
        text(7.5,5, velocity+’ km $\mathregular{s^{-1}}$’,color=’white’,fontsize=16)
        plot([-4.0],[-1.0], ’+’, markersize=8, markeredgewidth=1, color=’w’)
        cmap = imshow(img_chan[’image’][:][:][chan1],extent=[cxmin,cxmax,cymin,cymax],
        C1 = ax.contour(ra,dec,img_cont[’image’],levels=contlev,
        colors=’white’,width=4)

    if i==chan2:
        ax  = fig.add_subplot(1,2,2)
        ax.grid(False)
        velocity = ’%4.2f’ % (vel[chan2]-source)
        ax.axis([xmax,xmin,ymin,ymax],’scaled’)
        majorLocator = MultipleLocator(1.0)
        ax.xaxis.set_major_locator(majorLocator)
        ax.yaxis.set_major_locator(majorLocator)
        minorLocator= MultipleLocator(.5)
        ax.xaxis.set_minor_locator(minorLocator)
        ax.yaxis.set_minor_locator(minorLocator)
        text(7.5,5, velocity+’ km $\mathregular{s^{-1}}$’,color=’white’,fontsize=19)
        plot([-4.0],[-1.0], ’+’, markersize=8, markeredgewidth=1, color=’w’)
        cmap = imshow(img_chan[’image’][:][:][chan2],extent=[cxmin,cxmax,cymin,cymax],
```

```
        # Generate contour levels and plot contour map
        C1 = ax.contour(ra,dec,img_cont['image'],levels=contlev,
        colors='white',width=4)
        ax.set_xticklabels([])
        ax.set_yticklabels([])

# create color bar
cax = fig.add_axes([.9,0.12,0.03,0.78])
cbar = colorbar(cmap,cax=cax)
cbar.set_label('Jy $\mathregular{beam^{-1}}$', fontsize=16)
cbar.set_ticks(np.arange(cbmin,cbmax,cbtmaj))
#print(np.arange(cbmin,cbmax,cbtmaj))
minorLocator= LinearLocator(cbnum+1)
cbar.ax.yaxis.set_minor_locator(minorLocator)
cbar.update_ticks();
```

References

Adams, F.C., Lada, C.J. & Shu, F.H. (1987). Spectral evolution of young stellar objects. *The Astrophysical Journal*, **312**, 788–806. 9

Anglada, G., Rodríguez, L.F. & Torrelles, J.M. (1996). A thermal radio jet associated with the quadrupolar molecular outflow in l723. *The Astrophysical Journal Letters*, **473**, L123. 13

Anglada, G., Rodríguez, L.F. & Carrasco-González, C. (2018). Radio jets from young stellar objects. *The Astronomy and Astrophysics Review*, **26**, 3. 9, 13

Ao, Y., Henkel, C., Braatz, J., Weiss, A., Menten, K. & Mühle, S. (2011). Ammonia (j, k)=(1, 1) to (4, 4) and (6, 6) inversion lines detected in the seyfert 2 galaxy ngc 1068. *Astronomy & Astrophysics*, **529**, A154. 14, 68

Bally, J. (2007). Jets from young stars. *Astrophysics and Space Science*, **311**, 15–24. 9, 10, 14, 57, 67, 69

Bally, J. (2016). Protostellar outflows. *Annual Review of Astronomy and Astrophysics*, **54**, 491–528. 10, 13

Banerjee, R. & Pudritz, R.E. (2007). Massive star formation via high accretion rates and early disk-driven outflows. *The Astrophysical Journal*, **660**, 479. 8

Beltrán, M.T., Cesaroni, R., Codella, C., Testi, L., Furuya, R.S. & Olmi, L. (2006). Infall of gas as the formation mechanism of stars up to 20 times more massive than the sun. *Nature*, **443**, 427. 8, 9

BETZ, A. & MCLAREN, R. (1980). Infrared heterodyne spectroscopy of circumstellar molecules. In *Symposium-International Astronomical Union*, vol. 87, 503–508, Cambridge University Press. 17

BEUTHER, H. & WALSH, A. (2007). Kinematics of a hot massive accretion disk candidate. *The Astrophysical Journal Letters*, **673**, L55. 8, 9, 14, 15

BILLINGTON, S.J., URQUHART, J., FIGURA, C., EDEN, D. & MOORE, T. (2018). The rms survey: Ammonia mapping of the environment of young massive stellar objects ii. *Monthly Notices of the Royal Astronomical Society*, **483**, 3146–3167. 6, 46, 47

BRIGGS, D.S. (1995). High Fidelity Interferometric Imaging: Robust Weighting and NNLS Deconvolution. In *American Astronomical Society Meeting Abstracts*, vol. 27 of *Bulletin of the American Astronomical Society*, 1444. 25

BURNS, R., HANDA, T., NAGAYAMA, T., SUNADA, K. & OMODAKA, T. (2016). H2o masers in a jet-driven bow shock: episodic ejection from a massive young stellar object. *Monthly Notices of the Royal Astronomical Society*, **460**, 283–290. 17

BUTCHER, H.R., VAN BREUGEL, W., MILEY, G.K. *et al.* (1980). Optical observations of radio jets. *Astrophysical Journal*, **235**, 749. 9, 10

CASTANGIA, P., TARCHI, A., CACCIANIGA, A., SEVERGNINI, P., SURCIS, G. & DELLA CECA, R. (2017). A new jet/outflow maser in the nucleus of the compton-thick agn iras 15480-0344. *Proceedings of the International Astronomical Union*, **13**, 129–132. 16, 47

CASWELL, J., FULLER, G., GREEN, J., AVISON, A., BREEN, S., ELLINGSEN, S., GRAY, M., PESTALOZZI, M., QUINN, L., THOMPSON, M. *et al.* (2011). The 6-ghz methanol multibeam maser catalogue–iii. galactic longitudes 330 to 345. *Monthly Notices of the Royal Astronomical Society*, **417**, 1964–1995. 51

CESARONI, R., NERI, R., OLMI, L., TESTI, L., WALMSLEY, C. & HOFNER, P. (2005). A study of the keplerian accretion disk and precessing outflow in the massive protostar iras 20126+ 4104. *Astronomy & Astrophysics*, **434**, 1039–1054. 9

Cheung, A.C., Rank, D.M., Townes, C.H., Thornton, D.D. & Welch, W.J. (1968). Detection of nh_3 molecules in the interstellar medium by their microwave emission. *Phys. Rev. Lett.*, **21**, 1701–1705. 14

Cohen, M., Bieging, J. & Schwartz, P. (1982). Vla observations of mass loss from t tauri stars. *The Astrophysical Journal*, **253**, 707–715. 13

Consortium, A., Ainsworth, R.E., Scaife, A.M., Ray, T.P., Buckle, J.V., Davies, M., Franzen, T.M., Grainge, K.J., Hobson, M.P., Hurley-Walker, N. *et al.* (2012). Ami radio continuum observations of young stellar objects with known outflows. *Monthly Notices of the Royal Astronomical Society*, **423**, 1089–1108. 13

Csengeri, T., Bontemps, S., Wyrowski, F., Belloche, A., Menten, K. M., Leurini, S., Beuther, H., Bronfman, L., Commerçon, B., Chapillon, E., Longmore, S., Palau, A., Tan, J. C. & Urquhart, J. S. (2018). Search for high-mass protostars with alma revealed up to kilo-parsec scales (sparks) - i. indication for a centrifugal barrier in the environment of a single high-mass envelope. *A&A*, **617**, A89. 40

Curiel, S., Ho, P., Patel, N., Torrelles, J., Rodríguez, L., Trinidad, M., Cantó, J., Hernández, L., Gómez, J., Garay, G. *et al.* (2006). Large proper motions in the jet of the high-mass yso cepheus a hw2. *The Astrophysical Journal*, **638**, 878. 13

Dal Pino, E.M.d.G. (2005). Astrophysical jets and outflows. *Advances in Space Research*, **35**, 908–924. 7

Davidson, J., Novak, G., Matthews, T., Matthews, B., Goldsmith, P., Chapman, N., Volgenau, N., Vaillancourt, J. & Attard, M. (2011). Magnetic field structure around low-mass class 0 protostars: B335, l1527, and ic348-smm2. *The Astrophysical Journal*, **732**, 97. ix, 9, 11

Davies, B., Lumsden, S.L., Hoare, M.G., Oudmaijer, R.D. & de Wit, W.J. (2010). The circumstellar disc, envelope and bipolar outflow of the massive young stellar object w33a. *Monthly Notices of the Royal Astronomical Society*, **402**, 1504–1515. 6, 7

De Buizer, J.M., Walsh, A.J., Pina, R.K., Phillips, C.J. & Telesco, C.M. (2002). High-resolution mid-infrared imaging of g339. 88–1.26. *The Astrophysical Journal*, **564**, 327. 37

Dobaczewski, J., Nazarewicz, W. & Reinhard, P. (2014). Error estimates of theoretical models: a guide. *Journal of Physics G: Nuclear and Particle Physics*, **41**, 074001. 31, 44

Draper, P.W. (2014). SPLAT: Spectral Analysis Tool. Astrophysics Source Code Library. 47

Ellingsen, S., Norris, R. & McCulloch, P.M. (1996). Continuum emission associated with 6.7-ghz methanol masers. *Monthly Notices of the Royal Astronomical Society*, **279**, 101–107. 37, 40

Fedriani, R., Caratti o Garatti, A., Coffey, D., Garcia Lopez, R., Kraus, S., Weigelt, G., Stecklum, B., Ray, T. P. & Walmsley, C. M. (2018). Parsec-scale jets driven by high-mass young stellar objects - connecting the au- and the parsec-scale jet in iras 13481-6124. *Astronomy & Astrophysics*, **616**, A126. 31, 47, 48, 56, 66

Fleck Jr, R.C. (1988). Carbon monoxide as a tracer of molecular cloud mass and the question of cloud gravitational stability. *The Astrophysical Journal*, **333**, 840–844. 14

Friel, E. (1995). The old open clusters of the milky way. *Annual Review of Astronomy and Astrophysics*, **33**, 381–414. 2

Gao, Y. & Solomon, P.M. (2004). The star formation rate and dense molecular gas in galaxies. *The Astrophysical Journal*, **606**, 271. 14

Goddi, C., Moscadelli, L., Alef, W., Tarchi, A., Brand, J. & Pani, M. (2005). Kinematics of H_2O masers in high-mass star forming regions. *Astronomy & Astrophysics*, **432**, 161–173. 16, 50, 57, 67, 69

Greene, T.P. (2001). Protostars: ”stellar embryology” takes a step forward with the first detailed look at the youngest sun-like stars. *American Scientist*, **89**, 316–325. viii, 3

Guzman, A.E., Garay, G. & Brooks, K.J. (2010). A string of radio emission associated with IRAS 16562–3959: A collimated jet emanating from a luminous massive young stellar object. *The Astrophysical Journal*, **725**, 734. xi, 40, 41, 42, 43

Guzmán, A.E., Garay, G., Brooks, K.J., Rathborne, J. & Güsten, R. (2011). A hot molecular outflow driven by the ionized jet associated with iras 16562–3959. *The Astrophysical Journal*, **736**, 150. 40

Guzmán, A.E., Garay, G., Rodríguez, L.F., Moran, J., Brooks, K.J., Bronfman, L., Nyman, L.Å., Sanhueza, P. & Mardones, D. (2014). The slow ionized wind and rotating disklike system that are associated with the high-mass young stellar object g345. 4938+ 01.4677. *The Astrophysical Journal*, **796**, 117. 40, 41

Guzmán, A.E., Garay, G., Rodríguez, L.F., Contreras, Y., Dougados, C. & Cabrit, S. (2016). A protostellar jet emanating from a hypercompact h ii region. *The Astrophysical Journal*, **826**, 208. 5, 40, 41

Hennebelle, P. & Commerçon, B. (2014). Theories of the massive star formation: a (short) review. In *The Labyrinth of Star Formation*, 365–372, Springer. 6, 7

Ho, P.T. & Townes, C.H. (1983). Interstellar ammonia. *Annual Review of Astronomy and Astrophysics*, **21**, 239–270. 14, 15

Hosokawa, T. & Omukai, K. (2009). Evolution of massive protostars with high accretion rates. *The Astrophysical Journal*, **691**, 823. 5, 6

Ilee, J., Wheelwright, H., Oudmaijer, R., de Wit, W., Maud, L., Hoare, M., Lumsden, S., Moore, T., Urquhart, J. & Mottram, J. (2013). Co bandhead emission of massive young stellar objects: determining disc properties. *Monthly Notices of the Royal Astronomical Society*, **429**, 2960–2973. 32, 35

Jeans, B. (1902). I. the stability of a spherical nebula. *Phil. Trans. R. Soc. Lond. A*, **199**, 1–53. 4

Kraus, S., Hofmann, K.H., Menten, K.M., Schertl, D., Weigelt, G., Wyrowski, F., Meilland, A., Perraut, K., Petrov, R., Robbe-Dubois, S. *et al.* (2010). A hot compact dust disk around a massive young stellar object. *Nature*, **466**, 339. 32, 49, 67

Krauss, L.M. (2000). The age of globular clusters. *Physics Reports*, **333**, 33–45. 2

Krumholz, M.R., McKee, C.F. & Klein, R.I. (2004). How protostellar outflows help massive stars form. *The Astrophysical Journal Letters*, **618**, L33. 10

Kuiper, R. & Yorke, H.W. (2013). On the effects of optically thick gas (disks) around massive stars. *The Astrophysical Journal*, **763**, 104. 7

Kuiper, R., Klahr, H., Beuther, H. & Henning, T. (2011). Three-dimensional simulation of massive star formation in the disk accretion scenario. *The Astrophysical Journal*, **732**, 20. 9

Larson, R.B. (2003). The physics of star formation. *Reports on Progress in Physics*, **66**, 1651. 1

Lee, C.F., Li, Z.Y., Hirano, N., Shang, H., Ho, P.T.P. & Zhang, Q. (2018). ALMA observations of the very young class 0 protostellar system HH211-mms: A 30 au dusty disk with a disk wind traced by SO. *The Astrophysical Journal*, **863**, 94. ix, 12

LEUNG, C. & BROWN, R. (1977). On the interpretation of carbon monoxide self-absorption profiles seen toward embedded stars in dense interstellar clouds. *The Astrophysical Journal*, **214**, L73–L78. 14

LO, K. (2005). Mega-masers and galaxies. *Annu. Rev. Astron. Astrophys.*, **43**, 625–676. iv, 50, 52, 54, 58, 67, 70

LONGMORE, S., WALSH, A., PURCELL, C., BURKE, D., HENSHAW, J., WALKER, D., URQUHART, J., BARNES, A., WHITING, M., BURTON, M. *et al.* (2017). H_2O southern galactic plane survey (HOPS): Paper iii–properties of dense molecular gas across the inner milky way. *Monthly Notices of the Royal Astronomical Society*, **470**, 1462–1490. 46

LUMSDEN, S., HOARE, M., URQUHART, J., OUDMAIJER, R., DAVIES, B., MOTTRAM, J., COOPER, H. & MOORE, T. (2013). The red MSX source survey: The massive young stellar population of our galaxy. *The Astrophysical Journal Supplement Series*, **208**, 11. xii, xiii, 19, 20, 27, 30, 31, 35, 45, 51, 53, 60, 61, 62, 63, 64, 70

MCMULLIN, J., WATERS, B., SCHIEBEL, D., YOUNG, W. & GOLAP, K. (2007). Casa architecture and applications. In *Astronomical data analysis software and systems XVI*, vol. 376, 127. 22

MOTOGI, K., SORAI, K., HONMA, M., HIROTA, T., HACHISUKA, K., NIINUMA, K., SUGIYAMA, K., YONEKURA, Y. & FUJISAWA, K. (2016). Accelerating a water maser face-on jet from a high mass young stellar object. *Publications of the Astronomical Society of Japan*, **68**. 17

MOTTRAM, J.C., HOARE, M.G., DAVIES, B., LUMSDEN, S.L., OUDMAIJER, R.D., URQUHART, J.S., MOORE, T.J., COOPER, H.D. & STEAD, J.J. (2011). The rms survey: the luminosity functions and timescales of massive young stellar objects and compact H II regions. *The Astrophysical Journal Letters*, **730**, L33. 5

PARTRIDGE, B., LÓPEZ-CANIEGO, M., PERLEY, R., STEVENS, J., BUTLER, B., ROCHA, G., WALTER, B. & ZACCHEI, A. (2016). Absolute calibration of the radio astronomy flux density scale at 22 to 43 GHz using Planck. *The Astrophysical Journal*, **821**, 61. 23

Patel, N.A., Curiel, S., Sridharan, T., Zhang, Q., Hunter, T.R., Ho, P.T., Torrelles, J.M., Moran, J.M., Gómez, J.F. & Anglada, G. (2005). A disk of dust and molecular gas around a high-mass protostar. *Nature*, **437**, 109. 9

Pudritz, R. (1984). Star formation in rotating, magnetized molecular disks. In *Bulletin of the American Astronomical Society*, vol. 16, 877. 8, 9

Purcell, C., Longmore, S., Walsh, A., Whiting, M., Breen, S., Britton, T., Brooks, K., Burton, M., Cunningham, M., Green, J. *et al.* (2012). The h2o southern galactic plane survey: Nh3 (1, 1) and (2, 2) catalogues. *Monthly Notices of the Royal Astronomical Society*, **426**, 1972–1991. 46

Purser, S., Lumsden, S., Hoare, M., Urquhart, J., Cunningham, N., Purcell, C., Brooks, K., Garay, G., Gúzman, A. & Voronkov, M. (2016). A search for ionized jets towards massive young stellar objects. *Monthly Notices of the Royal Astronomical Society*, **460**, 1039–1053. x, 30, 32, 33, 34, 35, 36, 39, 66

Purser, S., Lumsden, S., Hoare, M. & Cunningham, N. (2017). Investigating the temporal domain of massive ionized jets–i. a pilot study. *Monthly Notices of the Royal Astronomical Society*, **475**, 2–19. 17, 37, 38, 40, 41, 43

Purser, S.J.D. (2017). *Ionised Jets Associated With Massive Young Stellar Objects*. Ph.D. thesis, University of Leeds. iv, 16, 18, 30, 31, 32, 34, 35, 37, 40, 43, 44, 45, 49, 50, 56, 66, 67, 69, 71

Reynolds, S.P. (1986). Continuum spectra of collimated, ionized stellar winds. *The Astrophysical Journal*, **304**, 713–720. 16

Rodriguez, L.F. (1997). Thermal radio jets. In *Symposium-International Astronomical Union*, vol. 182, 83–92, Cambridge University Press. 13

SAULT, R.J., TEUBEN, P. & WRIGHT, M.C. (2011). Miriad: multi-channel image reconstruction, image analysis, and display. *Astrophysics Source Code Library*. 22

URQUHART, J., HOARE, M.G., LUMSDEN, S.L., OUDMAIJER, R.D., MOORE, T.J., BROOK, P., MOTTRAM, J.C., DAVIES, B. & STEAD, J.J. (2009). The rms survey-h2o masers towards a sample of southern hemisphere massive yso candidates and ultra compact hii regions. *Astronomy & Astrophysics*, **507**, 795–802. xii, 46, 53, 61, 62, 68

URQUHART, J., FIGURA, C., MOORE, T., CSENGERI, T., LUMSDEN, S., PILLAI, T., THOMPSON, M., EDEN, D. & MORGAN, L. (2015). The rms survey: ammonia mapping of the environment of massive young stellar objects. *Monthly Notices of the Royal Astronomical Society*, **452**, 4029–4053. 1, 5, 6, 61, 68

VAN MOORSEL, G. (2014). The Very Large Array after the upgrade. In *General Assembly and Scientific Symposium (URSI GASS), 2014 XXXIth URSI*, 1–3, IEEE. 27

WALSH, A.J., BREEN, S., BRITTON, T., BROOKS, K., BURTON, M.G., CUNNINGHAM, M., GREEN, J., HARVEY-SMITH, L., HINDSON, L., HOARE, M.G. *et al.* (2011). The H_2O southern galactic plane survey (HOPS)–i. techniques and H_2O maser data. *Monthly Notices of the Royal Astronomical Society*, **416**, 1764–1821. xi, xii, 46, 50, 53, 56, 59

WHEELWRIGHT, H., DE WIT, W., OUDMAIJER, R., HOARE, M., LUMSDEN, S., FUJIYOSHI, T. & CLOSE, J. (2012). Probing the envelopes of massive young stellar objects with diffraction limited mid-infrared imaging. *Astronomy & Astrophysics*, **540**, A89. 35

WILSON, T.L., ROHLFS, K. & HÜTTEMEISTER, S. (2009). *Tools of radio astronomy*, vol. 5. Springer. 46

WILSON, W.E., FERRIS, R.H., AXTENS, P., BROWN, A., DAVIS, E., HAMPSON, G., LEACH, M., ROBERTS, P., SAUNDERS, S., KORIBALSKI, B.S. *et al.*

(2011). The Australia Telescope Compact array broad-band backend: Description and first results. *Monthly Notices of the Royal Astronomical Society*, **416**, 832–856. ix, 20

Wong, K., Menten, K., Kamiński, T., Wyrowski, F., Lacy, J. & Greathouse, T. (2018). Circumstellar ammonia in oxygen-rich evolved stars. *Astronomy & Astrophysics*, **612**, A48. 15

Yorke, H.W. & Sonnhalter, C. (2002). On the formation of massive stars. *The Astrophysical Journal*, **569**, 846. 9

Yu, N. & Wang, J.J. (2014). Molecular line study of massive star-forming regions from the red MSX source survey. *Monthly Notices of the Royal Astronomical Society*, **440**, 1213–1224. 30

Zinnecker, H. & Yorke, H.W. (2007). Toward understanding massive star formation. *Annu. Rev. Astron. Astrophys.*, **45**, 481–563. 6, 7